Article

Cell

Small Molecule Targets TMED9 and Promotes Lysosomal Degradation to Reverse Proteinopathy

Graphical Abstract

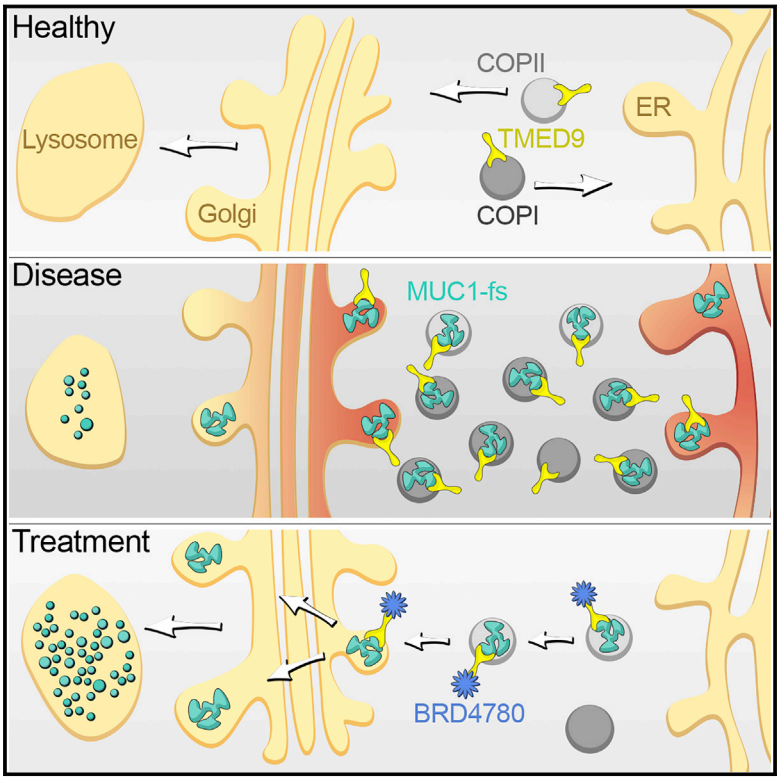

Highlights

- Mutant MUC1-fs is toxic to kidney cells by accumulating in TMED9-enriched vesicles
- BRD4780 binds cargo receptor TMED9, releases MUC1-fs, and re-routes it to lysosome
- MUC1-fs is cleared from kidneys of knockin mice and patient kidney organoids
- BRD4780 is a promising lead for the treatment of toxic proteinopathies

Authors

Moran Dvela-Levitt, Maria Kost-Alimova, Maheswarareddy Emani, ..., Todd R. Golub, Eric S. Lander, Anna Greka

Correspondence

agreka@broadinstitute.org

In Brief

A small molecule shows promise in clearing misfolded proteins by re-routing them toward lysosomal degradation.

Dvela-Levitt et al., 2019, Cell *178*, 521–535
July 25, 2019
https://doi.org/10.1016/j.cell.2019.07.002

CellPress

Cell

Small Molecule Targets TMED9 and Promotes Lysosomal Degradation to Reverse Proteinopathy

Moran Dvela-Levitt,[1,2] Maria Kost-Alimova,[1] Maheswarareddy Emani,[1,2] Eva Kohnert,[1,2] Rebecca Thompson,[1,2] Eriene-Heidi Sidhom,[1,2] Ana Rivadeneira,[1,2] Nareh Sahakian,[1,2] Julie Roignot,[1,2] Gregory Papagregoriou,[3] Monica S. Montesinos,[1,2] Abbe R. Clark,[1,2] David McKinney,[1] Juan Gutierrez,[1] Mark Roth,[1] Lucienne Ronco,[1] Esther Elonga,[1] Todd A. Carter,[1] Andreas Gnirke,[1] Michelle Melanson,[1] Kate Hartland,[1] Nicolas Wieder,[1,2] Jane C.-H. Hsu,[1] Constantinos Deltas,[3] Rebecca Hughey,[5] Anthony J. Bleyer,[6,7] Stanislav Kmoch,[6,7] Martina Živná,[7] Veronika Barešova,[7] Savithri Kota,[8] Johannes Schlondorff,[8] Myriam Heiman,[1,9] Seth L. Alper,[8] Florence Wagner,[1] Astrid Weins,[2,4] Todd R. Golub,[1] Eric S. Lander,[1,10,11] and Anna Greka[1,2,12,*]

[1]Broad Institute of MIT and Harvard, Cambridge, MA, USA
[2]Department of Medicine, Brigham and Women's Hospital and Harvard Medical School, Boston, MA, USA
[3]Molecular Medicine Research Center and Laboratory of Molecular and Medical Genetics, Department of Biological Sciences, University of Cyprus, Nicosia, Cyprus
[4]Department of Pathology, Brigham and Women's Hospital, Boston, MA, USA
[5]Renal-Electrolyte Division, Department of Medicine, University of Pittsburgh School of Medicine, Pittsburgh, PA, USA
[6]Section on Nephrology, Wake Forest School of Medicine, Medical Center Blvd., Winston-Salem, NC, USA
[7]Research Unit for Rare Diseases, Department of Pediatrics and Adolescent Medicine, First Faculty of Medicine, Charles University, Prague, Czech Republic
[8]Department of Medicine, Beth Israel Deaconess Medical Center and Harvard Medical School, Boston, MA, USA
[9]The Picower Institute for Learning and Memory, Department of Brain and Cognitive Sciences, MIT, Cambridge, MA, USA
[10]Department of Biology, MIT, Cambridge, MA, USA
[11]Department of Systems Biology, Harvard Medical School, Boston, MA, USA
[12]Lead Contact
*Correspondence: agreka@broadinstitute.org
https://doi.org/10.1016/j.cell.2019.07.002

SUMMARY

Intracellular accumulation of misfolded proteins causes toxic proteinopathies, diseases without targeted therapies. Mucin 1 kidney disease (MKD) results from a frameshift mutation in the *MUC1* gene (MUC1-fs). Here, we show that MKD is a toxic proteinopathy. Intracellular MUC1-fs accumulation activated the ATF6 unfolded protein response (UPR) branch. We identified BRD4780, a small molecule that clears MUC1-fs from patient cells, from kidneys of knockin mice and from patient kidney organoids. MUC1-fs is trapped in TMED9 cargo receptor-containing vesicles of the early secretory pathway. BRD4780 binds TMED9, releases MUC1-fs, and reroutes it for lysosomal degradation, an effect phenocopied by TMED9 deletion. Our findings reveal BRD4780 as a promising lead for the treatment of MKD and other toxic proteinopathies. Generally, we elucidate a novel mechanism for the entrapment of misfolded proteins by cargo receptors and a strategy for their release and anterograde trafficking to the lysosome.

INTRODUCTION

Diseases associated with protein misfolding and aggregation are known as proteinopathies (Bayer, 2015). More than 50 proteinopathies are caused by genetic mutations that result in protein misfolding and intracellular accumulation (Dubnikov et al., 2017; Dugger and Dickson, 2017). The accumulated proteins can cause cellular toxicity as seen in some forms of amyotrophic lateral sclerosis (ALS), Parkinson's disease, and retinitis pigmentosa (RP) (Dubnikov et al., 2017; Dugger and Dickson, 2017). Some proteinopathies, such as RP (Athanasiou et al., 2018), are characterized by the accumulation of misfolded proteins in the secretory pathway (endoplasmic reticulum [ER] and Golgi apparatus), whereas others, such as Huntington's disease (Zoghbi and Orr, 2000), involve accumulation of misfolded protein aggregates in the cytoplasm or the nucleus.

The early secretory pathway of eukaryotic cells is composed of three organelles: the ER, the ER-Golgi intermediate compartment (ERGIC), and the Golgi apparatus (Gomez-Navarro and Miller, 2016). The ER is a multifunctional organelle that orchestrates the synthesis, folding, and structural maturation of nearly one-third of all cellular proteins (Hetz et al., 2015). The Golgi apparatus occupies a central position within the secretory pathway, acting as a hub for vesicular trafficking. Distinct classes of vesicles transport diverse cargoes into and out of this organelle, as well as between the *cis*- and trans-Golgi subcompartments (Gomez-Navarro and Miller, 2016; Witkos and Lowe, 2017). Maintenance of the ER and Golgi apparatus requires a balance of anterograde coat protein II (COPII)-mediated and retrograde (COPI)-mediated vesicular trafficking (Gomez-Navarro and Miller, 2016). Together, the ER and the Golgi are responsible for biogenesis and proper intracellular distribution of a wide range of proteins (Gomez-Navarro and Miller, 2016).

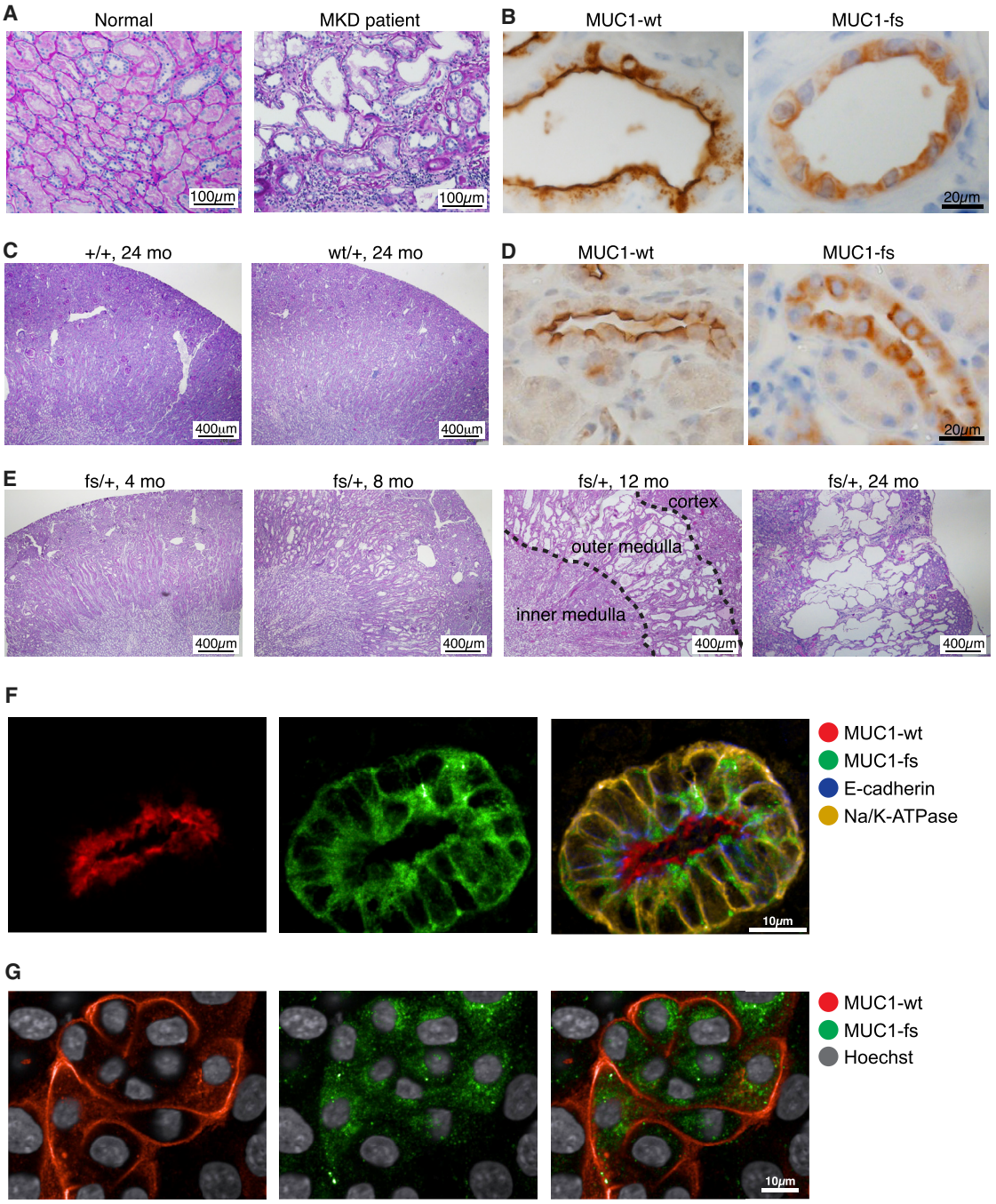

Figure 1. Mutant MUC1-fs Is Retained Intracellularly in Kidney Tubular Epithelial Cells

(A) Periodic acid-schiff (PAS) staining of kidney biopsies from a normal individual (left) and an MKD patient (right).

(B) Immunoperoxidase staining for MUC1-wt protein (apical tubular cell staining, left) and MUC1-fs protein (diffuse intracellular tubular cell staining, right) in an MKD patient kidney biopsy.

(C) PAS-stained kidney sections from 24-month-old +/+ and wt/+ female knockin mice, serving as a negative control (n = 67 +/+ mice; 23 wt/+ mice).

(D) Immunoperoxidase staining for MUC1-wt protein (apical, left) and MUC1-fs protein (diffuse intracellular, right) from a fs/+ knockin mouse shows similar localization as in human MKD kidney tissue (B, above).

(E) PAS-stained kidney sections from female fs/+ knockin mice at ages 4, 8, 12, and 24 months old, illustrating progressively prominent dilated tubules. Kidney regions (cortex, medulla) marked with dashed lines (n = 23 fs/+ mice).

(legend continued on next page)

The unfolded protein response (UPR) is activated upon increased secretory protein load to ensure maintenance of cellular homeostasis (Brandizzi and Barlowe, 2013; Plate and Wiseman, 2017; Walter and Ron, 2011). Mutant proteins disrupt the secretory pathway and trigger the UPR (Walter and Ron, 2011). The three principal branches of the UPR—IRE1 (inositol requiring enzyme), PERK (PKR-like ER kinase), and ATF6 (activating transcription factor 6)—work together to maintain ER homeostasis (Walter and Ron, 2011). However, in the setting of excess or prolonged cellular stress, the protective capacity of the UPR may be insufficient to restore homeostasis, triggering the induction of cell death (Walter and Ron, 2011), a hallmark of many proteinopathies (Remondelli and Renna, 2017).

Autosomal dominant tubulo-interstitial kidney disease-*mucin1* (ADTKD-*MUC1* or *MUC1* kidney disease, MKD) is caused by a frameshift mutation in the GC-rich variable number of tandem repeats (VNTR) region of the *MUC1* gene (Kirby et al., 2013). MKD is characterized by slowly progressive tubulo-interstitial disease that leads to kidney failure (Bleyer et al., 2017; Yu et al., 2018).

The *MUC1* gene encodes the transmembrane glycoprotein mucin 1 (MUC1), which is expressed at the apical surface of glandular or luminal epithelial cells in the mammary gland, digestive tract, uterus, prostate, lung, and kidney (Hattrup and Gendler, 2008) or in epithelial cancers (Nath and Mukherjee, 2014). In the kidney, MUC1 localizes to distal convoluted tubules and collecting duct (Leroy et al., 2002), while following ischemia, the protein may be induced in the proximal tubule (Al-Bataineh et al., 2016; Gibier et al., 2017).

In all known cases of MKD, the causative mutations result in the same frameshift, producing a mutant MUC1 neo-protein (MUC1-fs) (Kirby et al., 2013; Wenzel et al., 2018; Yamamoto et al., 2017; Živná et al., 2018). The vast majority of these mutations involve the insertion of an extra cytosine in a string of seven cytosines within one of the VNTR subunits (Kirby et al., 2013). MUC1-fs retains the wild-type N-terminal signal sequence that drives ER translation, but beyond the insertion, it has tandem series of novel 20 amino acid imperfect repeats and a C-terminal neo-peptide with an early stop codon, resulting in the absence of the transmembrane and intracellular domains found in the wild-type MUC1 protein (Kirby et al., 2013) (Figures S1A and S1B). To date, the molecular mechanism responsible for MKD is unknown, and no therapy is available.

Here, we show that intracellular accumulation of MUC1-fs in early secretory compartments leads to activation of the UPR. Mutant MUC1-fs is trapped in TMED9 cargo receptor-enriched compartments of the early secretory pathway in patient cells, knockin mouse kidneys, and patient induced pluripotent stem cell (iPSC)-derived kidney organoids. We describe the identification of a small molecule, BRD4780, that releases MUC1-fs from TMED9-enriched compartments and promotes its anterograde trafficking to the lysosome. TMED9 deletion phenocopied the effect of BRD4780. Our findings elucidate a fundamental cellular mechanism for misfolded protein entrapment and identify BRD4780 as a promising lead for the treatment of toxic proteinopathies.

RESULTS

Mutant MUC1-fs Is Retained Intracellularly in Tubular Epithelial Cells

We characterized the location of the wild-type (MUC1-wt) and mutant (MUC1-fs) proteins in a kidney biopsy from a 50-year-old MKD patient, who was a heterozygous carrier for a C insertion frameshift mutation (*MUC1*^{wt}/*MUC1*^{fs}). As compared to normal kidney (Figure 1A, left), the patient's tissue showed tubular atrophy, tubular dilation, and some interstitial fibrosis (Figure 1A, right). We visualized MUC1-wt and MUC1-fs proteins by immunoperoxidase staining with wild-type- and mutant-specific antibodies in the same kidney biopsy. MUC1-wt maintained its normal localization at the apical membrane of distal tubules and collecting ducts, whereas MUC1-fs showed intracellular accumulation (Figure 1B).

We generated heterozygous knockin mice in which one of the normal mouse *mMuc1*^{wt} (+) alleles was replaced with either a human wild-type (*hMUC1*^{wt} or wt) or mutant (*hMUC1*^{fs} or fs) allele (Figures S1Aand S1B). For clarity, we indicate the knockin mice as wt/+ or fs/+ as compared to +/+ for the parental wild-type mouse line. We confirmed expression of the corresponding human protein using western blot (Figure S1C) and immunohistochemistry (IHC) (Figure S1D). IHC in fs/+ heterozygous mice demonstrated that the distribution of the normal and mutant MUC1 proteins was consistent with the pattern seen in kidney biopsies from MKD patients (Figure 1B): normal MUC1-wt protein was found at the plasma membrane of tubular epithelial cells, and the mutant MUC1-fs protein was found intracellularly (Figure 1D).

While no pathologic changes were detected in kidneys from the parental strain (+/+) or mice carrying the normal human allele (wt/+) (Figure 1C), mice carrying the mutant allele (fs/+) developed progressive kidney disease (Figure 1E). The pathological changes detected in fs/+ mice were similar to those observed in MKD patient biopsies, marked by tubular dilations and some interstitial fibrosis (Figure 1E). This kidney pathology developed as early as 8 months of age in female fs/+ mice (Figure 1E) compared to male mice, in which tubular pathology was noted at 12 months of age (Figure S1F). Serum creatinine was mildly elevated in female fs/+ mice at 76 weeks of life and beyond, but not in males (Figure S1E; Table S1). We characterized the distribution of normal mouse and mutant human MUC1 proteins in different segments of the kidney by double labeling immunofluorescence (IF) microscopy with segment-specific markers (Figure S2A). Both MUC1-fs and MUC1-wt were expressed in sodium-chloride symporter (NCC or SLC12A3)-positive distal convoluted tubules and aquaporin 2 (AQP2)-positive collecting ducts in the cortex and inner medulla, whereas Lotus

(F) IF co-staining of distal tubule in MKD patient kidney organoid for MUC1-wt (red), MUC1-fs (green), E-cadherin (blue), and Na^+/K^+-ATPase (yellow). MUC1-fs localized intracellularly (middle) compared to apical MUC1-wt (left).

(G) IF co-staining in P cells for MUC1-fs (green), MUC1-wt (red), and Hoechst (gray). MUC1-fs localized intracellularly (middle) compared to MUC1-wt on the plasma membrane (left).

See also Figures S1, S2, and S3 and Table S1.

tetragonolobus lectin (LTL)-positive proximal tubules in the outer medulla expressed solely MUC1-fs (Figure S2A). This finding was of interest because the outer medulla is the kidney region in which the mutant mice exhibited the earliest and ultimately most severe histopathological changes (Figures 1E and S2B).

We also generated human kidney organoids (Morizane and Bonventre, 2017; Takasato et al., 2016) from MKD patient iPSCs. The iPSCs were made from erythroblasts obtained from three MKD patients. iPSCs from unaffected siblings served as controls. Mature organoids (29 days, see STAR Methods) developed nephron structures including proximal and distal tubules, as we recently characterized in detail (Subramanian et al., 2019). MUC1-wt was detected in normal, sibling-derived, and patient-derived kidney organoids, at highest abundance in distal nephron structures (Figure S3A). In line with previous observations in MKD patient kidney biopsies (Bleyer et al., 2017; Yu et al., 2018), MUC1-fs was observed exclusively in MKD patient-derived organoids, in E-cadherin and Na/K-ATPase-positive tubules, and to a lesser extent, in LTL-positive tubules (Figures 1F and S4A). Notably, MUC1-wt was located at the apical membrane of these tubules (Figure 1F), whereas MUC1-fs was localized intracellularly (with basolateral membranes defined by Na/K ATPase staining; Figure 1F). Thus, human organoids recapitulate the subcellular localization of MUC1-wt and MUC1-fs as seen in human kidney biopsies.

To enable downstream mechanistic studies, we generated an immortalized tubular epithelial cell line from a patient with MKD (P cells) and compared MUC1 expression to a cell line derived from a normal human kidney (N cells; Figures S3B and S3C). P cells expressed MUC1-wt on the plasma membrane (Figure 1G), similar to N cells (Figure S3B), whereas MUC1-fs was found exclusively in P cells (Figures S3B and S3C) in a diffuse intracellular, perinuclear pattern similar to that previously seen in patient kidney biopsies, iPSC-derived kidney organoids, and knockin mouse kidneys (Figure 1G).

MUC1-fs Accumulation Triggers the ATF6 Branch of the UPR

To decipher the molecular mechanism by which MUC1-fs accumulation alters epithelial cell function, we analyzed the involvement of the UPR, a prominent mechanism for the regulation of cellular proteostasis (Plate and Wiseman, 2017). First, to address the involvement of IRE1, PERK, and ATF6 branches of the UPR (Walter and Ron, 2011) in P cells, we analyzed RNA sequencing (RNA-seq) data from P and N cells using published transcriptional signatures of either general or branch-specific UPR activation (Adamson et al., 2016). This analysis indicated general activation of the UPR (Complex), and clear, significant upregulation of the ATF6 branch (Figure 2A). Minimal transcriptional changes were noted in the IRE1 and PERK branches (Figures 2A).

Since the activation of specific UPR branches can promote either cytoprotective or proapoptotic outputs (Hetz, 2012), we tested their involvement in P cell viability by inhibiting one branch at a time (Figures S3D–S3F). MUC1-fs accumulation alone did not induce apoptosis (as measured by caspase 3/7 activity; Figures 2B and S3G). However, the inhibition of ATF6 resulted in increased apoptosis in P cells compared to N cells (Figure 2B), suggesting that the ATF6 UPR branch might be specifically upregulated to protect P cells from MUC1-fs-induced toxicity. Consistent with this, ATF6 inhibition also caused enhanced accumulation of MUC1-fs in P cells (Figure S3H). IRE1 inhibition induced apoptosis broadly, in line with its general cytoprotective role (Ishikawa et al., 2019; Lin et al., 2007), with no significant difference between P and N cells (Figure 2B). PERK inhibition had no effect on apoptosis (Figure 2B). Together, these results support the notion that ATF6 is activated to counteract MUC1-fs accumulation and associated toxicity. We validated these results by measuring the abundance of the main downstream sensor proteins of the three UPR branches. Consistent with the RNA-seq data (Figure 2A), we observed upregulation of BiP, a chaperone activated by all three UPR branches (Figure 2C). The activation of the ATF6 branch was verified by the increased abundance of ERp72 and GRP94 (Figure 2C). In keeping with the above results, we detected minimal changes in ATF4, the main transcription factor of the PERK pathway, or CHOP, the proapoptotic target gene of ATF4 (Figure 2C). We also did not detect XBP1 mRNA splicing, a key step in the activation of the IRE1 pathway (Figure 2C).

Given the increased vulnerability of P cells to ATF6 inhibition, we reasoned that increased stress signaling through the activation of the PERK and IRE1 arms of the UPR may further promote tubular cell injury. We therefore tested the effect of thapsigargin (THP), a well-known ER stressor, on P cells and found higher susceptibility to apoptosis compared to N cells (Figures S3I and S3J). Consistent with this, treatment with THP triggered the proapoptotic PERK pathway specifically in P cells, as shown by increased ATF4 and CHOP abundance (Figure 2D). XBP1 splicing was also noted in P cells after treatment with THP (Figure 2D). Taken together, these results suggest that THP-induced activation of the UPR drives P cell apoptosis, thus defining a cell-based assay valuable for downstream drug screening efforts.

The UPR pathways were also relevant *in vivo*. In kidneys of fs/+ mice, the ATF6 marker ERp72 was most abundant in the same tubular structures as MUC1-fs in the outer medulla (Figure 2E). Furthermore, we found increased protein abundance of calreticulin, ERp72, GRP94, and CHOP in tissue lysates from kidneys of 12-month-old fs/+ mice (Figure 2F). The increased abundance of proapoptotic CHOP was associated with increased apoptosis in 12-month-old mice, as evidenced by positive terminal deoxynucleotidyl transferase dUTP nick end labeling (TUNEL) staining primarily in the outer medulla of kidneys from fs/+ mice (Figures 2G and 2H).

BRD4780 Selectively Clears Mutant but Not Wild-type MUC1

To identify compounds that can remove MUC1-fs, we developed a high-content screen (HCS) using an IF cell-based assay that could simultaneously assess the abundance of MUC1-wt, MUC1-fs, and cell number in a 384-well format utilizing a fully automated staining protocol and confocal imaging microscopy system (*Z* score 0.35, Figure S4A). We screened the Broad Repurposing Library, a set of 3,713 compounds at different stages of preclinical and clinical development (Corsello et al., 2017) (Figures 3A and S4A). The bromodomain inhibitor JQ1 was used as a positive control because preliminary *in vitro* experiments in P cells showed that it results in 100% transcriptional suppression of both MUC1-fs and MUC1-wt.

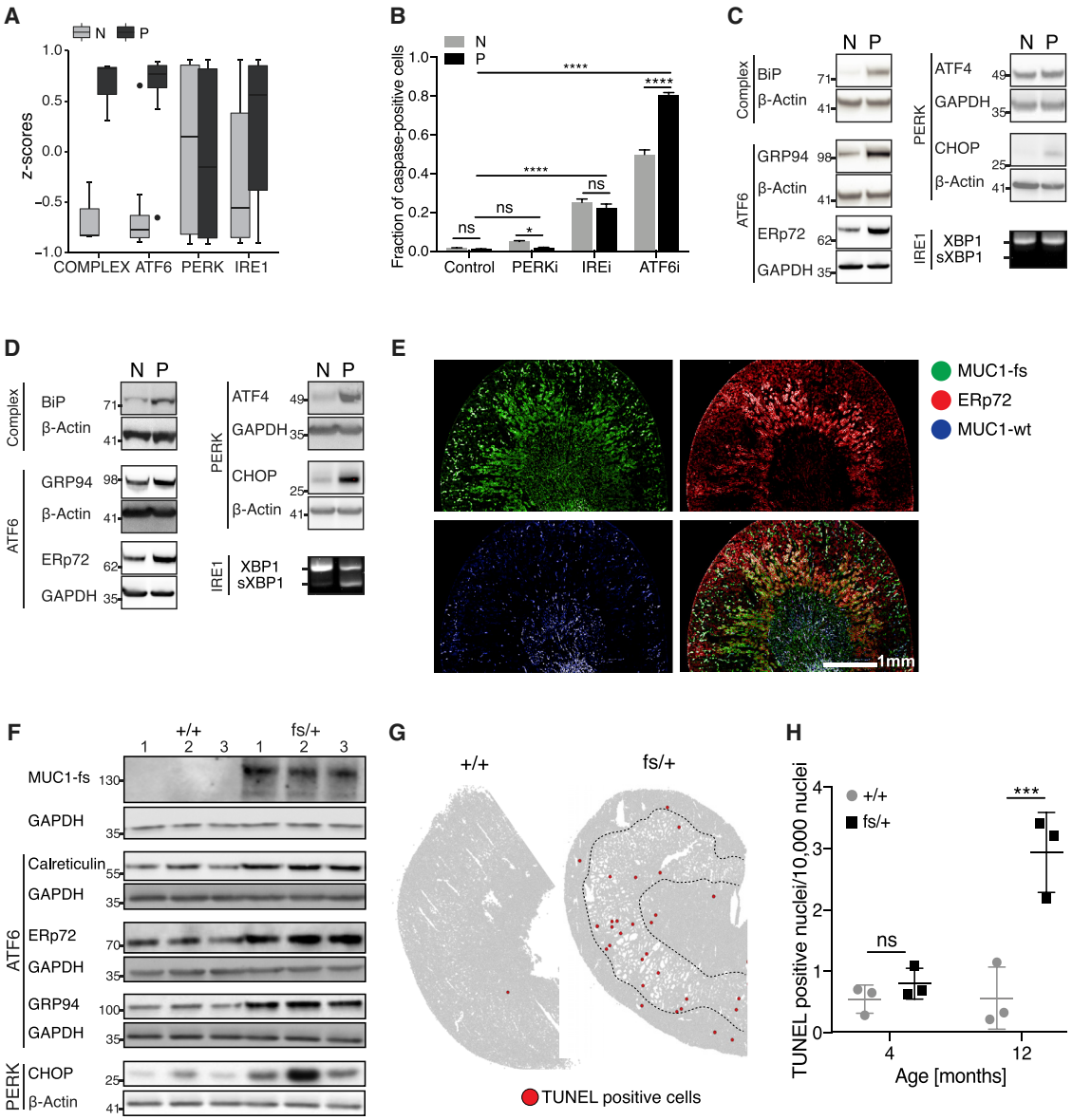

Figure 2. MUC1-fs Accumulation Triggers the ATF6 Branch of the UPR

(A) UPR branch activation analysis in N and P cells. Generalized (Complex) or specific branch activation (ATF6, PERK, and IRE1) was evaluated. *Z* scores of normalized expression values obtained from RNA-seq were used to generate scaled mean expression profiles (n = 3 replicates). *p < 0.05.

(B) Inhibition of the three UPR branches demonstrates a specific involvement of ATF6 in P cell cytoprotection. Cell apoptosis after 72 h treatment with either PERK inhibitor (PERKi, GSK2656157, 10 μM), IRE inhibitor (IREi, 4μ8c, 10 μM), or ATF6 inhibitor (ATF6i, PF-429242, 10 μM). Caspase 3/7 activation was calculated as the fraction of caspase 3/7 positive cells. Means ± SD (n = 4 replicates). *p < 0.05; ****p < 0.0001.

(C) Immunoblot and RT-PCR analysis of downstream effectors of the three UPR branches. Protein abundance of BiP (Complex), GRP94 and ERp72 (ATF6), ATF4 and CHOP (PERK), and mRNA levels of spliced XBP1 (sXBP1; IRE) are consistent with trends in transcriptomic data in (A) and cell protection data in (B) (n > 3 replicates).

(D) Activation of UPR branch downstream effectors (as described in C) after treatment with THP (100 nM) for 12 h (n > 3 replicates).

(E) Low-magnification IF images of kidney section stained for MUC1-wt (blue), MUC1-fs (green), and ERp72 (red) in 4-month-old female fs/+ mice (before disease onset). Co-staining of MUC1-fs with the ATF6 effector ERp72 in tubules of the outer medulla.

(F) Immunoblot analysis of MUC1-fs and UPR downstream effectors in 12-month-old female +/+ and fs/+ mice (advanced disease). Increased abundance of calreticulin, ERp72 and GRP94 (ATF6 branch), and CHOP (PERK branch) observed in fs/+ mice (n = 3 mice/genotype).

(G) Digital illustration of representative kidney sections stained with TUNEL to detect apoptotic cells in 12-month-old female +/+ and fs/+ mice (advanced disease). All cells detected in the tissue section are plotted according to their position on tissue slide (gray dots). Increased number of TUNEL-positive cells (red dots) in fs/+ kidney section mainly in area of tubular damage (dashed line).

(H) Increased apoptosis in 12-month-old female fs/+ mice versus female +/+ mice as indicated by TUNEL staining quantification. Means ± SD (n = 3 mice/genotype). ns, p > 0.05; ***p < 0.001.

See also Figure S3.

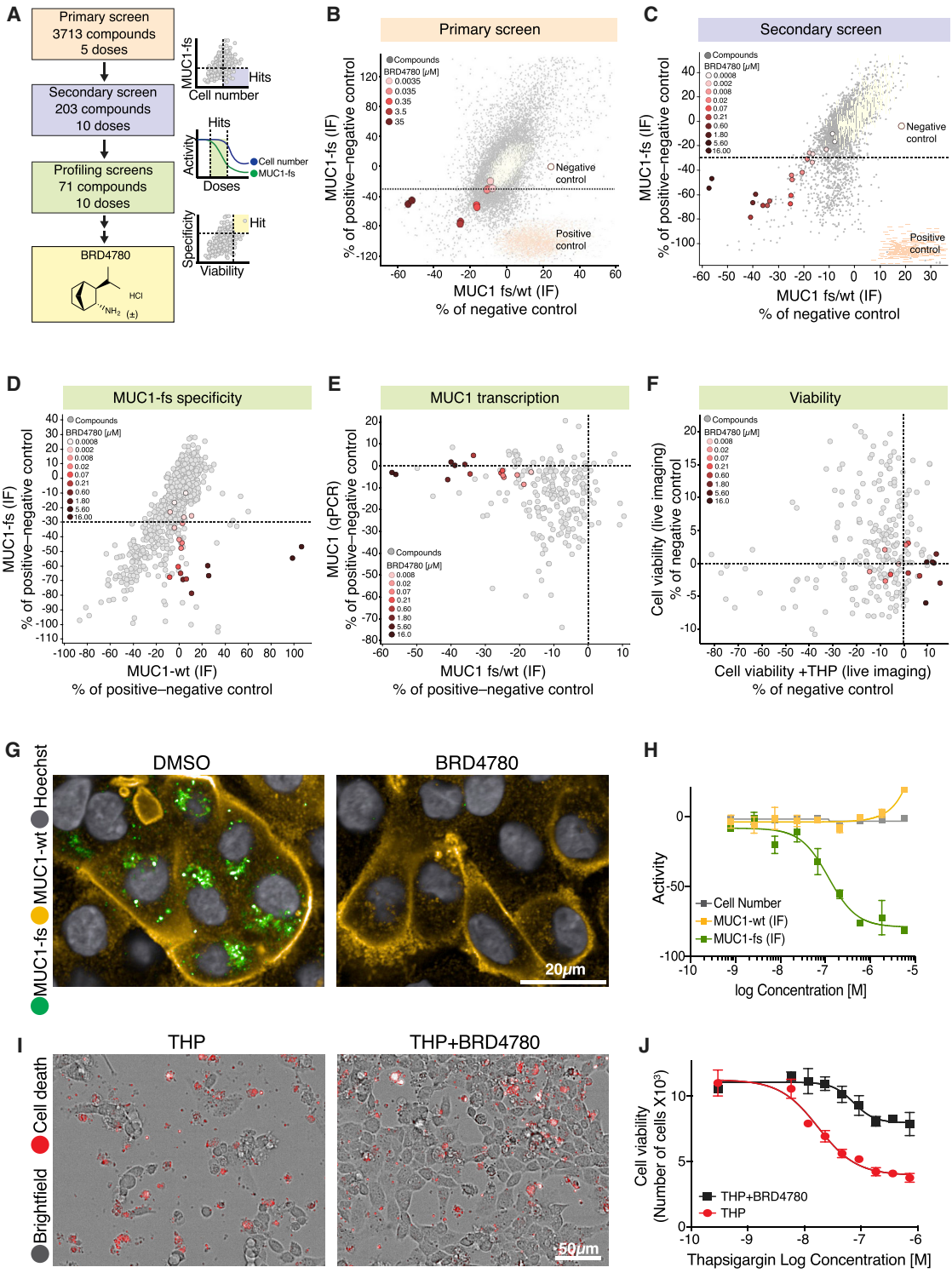

Figure 3. BRD4780 Clears Mutant MUC1-fs

(A) A schematic illustration demonstrating the HCS screening strategy resulting in the identification of BRD4780.

(B) Primary screen results showing IF quantification of MUC1-fs versus MUC1 fs/wt ratio in P cells treated for 48 h with each of 3,713 compounds of the Re-purposing Library at 5 dose points. DMSO (light yellow) was the negative control; JQ1 (orange) was the positive control. All compounds are marked in gray, and progressively higher concentrations of BRD4780 are highlighted with a pink-to-red dot color gradient (also in C–F).

(legend continued on next page)

For the primary screen, we tested the Repurposing Library at 5 doses (Figures 3A and 3B), with positive hits defined by (1) reduction of MUC1-fs by >30% at a minimum of two consecutive compound doses and (2) lack of cell toxicity at these doses (no significant reduction in cell number). A total of 203 compounds (5%) met these criteria (Figure 3B). We retested these compounds in a secondary screen, generating dose-response curves at 10 doses and defining positive hits based on the same two criteria as for the primary screen. A total of 71 compounds were selected for further evaluation (Figures 3A and 3C). While many of the compounds caused comparable reduction of both MUC1-fs and MUC1-wt, we noticed that some preferentially removed MUC1-fs (Figures 3B and 3C). We further characterized the 71 compounds in three assays: (1) we tested compound specificity for MUC1-fs reduction (Figure 3D), (2) we measured MUC1 mRNA levels to eliminate compounds that reduced MUC1 protein abundance through transcriptional suppression (MUC1-wt and MUC1-fs mRNAs are not readily distinguished and are transcribed from the same promoter; Figure 3E), and (3) we tested whether compounds could rescue P cells from cell death caused by THP (Figure 3F).

A single compound, BRD4780, emerged from these three profiling assays (Figure 3A). First, BRD4780 resulted in dose-dependent removal (EC_{50} = 143 nM) of mutant MUC1-fs without decreasing wild-type MUC1 (Figures 3G and 3H). Second, BRD4780 showed no effect on MUC1 transcriptional regulation (Figure 3E). Third, BRD4780 rescued P cells from THP-induced cell death (Figures 3I and 3J) and significantly reduced UPR activation (Figure S4B). Taken together, the high-content screening and profiling assays identified BRD4780 as a compound that selectively reduced mutant but not wild-type MUC1.

BRD4780 Removes Mutant MUC1-fs from Kidneys of Heterozygous Knockin Mice

We next tested whether BRD4780 could reverse the accumulation of MUC1-fs *in vivo*. Based on PK studies in male 129S2 mice (Figures S4C and S4D), we administered the compound (1, 10, and 50 mg/kg) or vehicle to 8-month-old male heterozygous knockin (fs/+) mice by daily oral gavage for 7 days. Following treatment, mice were sacrificed, and their kidneys were harvested and processed to assess MUC1-fs protein abundance by IF (Figures 4A and 4B) and western blot (Figure 4C). BRD4780 treatment resulted in a dose-dependent removal of mutant MUC1-fs protein from mouse kidneys (Figures 4B and 4C). At the highest dose (50 mg/kg), we noted such efficient removal of mutant MUC1-fs that the tissue appeared nearly indistinguishable from control (+/+) mouse kidneys (Figure 4A). Consistent with *in vitro* data, BRD4780 had no effect on MUC1-wt (Figures 4A and S4E). In addition to removing the toxic mutant protein, BRD4780 treatment downregulated pathways associated with ER stress and the UPR, as shown by pathway analysis of bulk RNA-seq data (Figure 4D; see STAR Methods).

BRD4780 Removes MUC1-fs Protein from Patient iPSC-Derived Kidney Organoids

To confirm the human relevance of these findings, we evaluated the effect of BRD4780 on MUC1-fs in kidney organoids generated from iPSCs of patients with MKD. Using single-cell genomics and IF, we recently reported a comprehensive characterization of iPSC-derived human k'idney organoids and confirmed their reproducibility and potential utility for drug discovery (Subramanian et al., 2019). Here, we tested the effect of BRD4780 on MUC1-fs protein levels in kidney organoids derived from iPSCs of three patients with MKD (P1–P3) compared to organoids derived from an unaffected control (N1). BRD4780 cleared the mutant protein from intracellular compartments in all patient organoids (Figures 5A, 5B, and S4F), while MUC1-wt protein levels in patient or control organoids remained unchanged (Figures 5A and 5C). These results support the human relevance of our findings.

MUC1-fs Accumulates in the Early Secretory Pathway, in a TMED9 Cargo Receptor-Positive Compartment

MUC1-wt is a transmembrane glycoprotein, with a signal peptide (SP) (Figure S1B) that directs it to the secretory pathway (Nath and Mukherjee, 2014). Newly synthesized MUC1-wt is transported from the ER to the Golgi apparatus for O-glycosylation prior to its delivery to the apical plasma membrane (Apostolopoulos et al., 2015). Like all transmembrane proteins, MUC1-wt is packaged into COPII vesicles and is transported from the ER to the Golgi apparatus (Gomez-Navarro and Miller, 2016). At this point, cells can distinguish between wild-type

(C) Secondary screen results showing IF quantification of MUC1-fs versus MUC1 fs/wt ratio in P cells treated for 48 h with each of 203 compounds (identified as hits from the primary screen) at 10 dose points. DMSO (light yellow), negative control; JQ1 (orange), positive control.

(D) MUC1-fs profiling assay showing IF quantification of MUC1-fs versus MUC1-wt in P cells treated for 48 h at 10 dose points with each of 71 compounds derived from the secondary screen.

(E) MUC1 transcription assay showing measurement of total MUC1 mRNA versus IF quantification of MUC1 fs/wt ratio in P cells treated for 24 h and 48 h, respectively, with 71 compounds from the secondary screen. Only doses active in removing MUC1-fs are shown.

(F) Cell viability assay showing quantification for P cells treated with 71 compounds from the secondary screen with or without THP (100 nM). Only doses active in removing MUC1-fs are shown. Cell viability was measured using live imaging, followed by measuring the fraction of live cells (cells negative for caspase 3/7 and DRAQ7).

(G) IF images of P cells treated for 48 h with DMSO or BRD4780 (5 μM). MUC1-wt, yellow; MUC1-fs, green; Hoechst, gray.

(H) BRD4780 dose-response curves for IF-detected MUC1-fs, MUC1-wt, and cell number in P cells treated as in (G). Solid lines represent the best fits of the data to the four-parameter dose-response curve (GraphPad Prism software). EC_{50} = 143 nM. Means ± SD.

(I) Bright field images of representative P cells pretreated for 48 h with BRD4780 (5 μM) or DMSO followed by 5 days co-treatment with BRD4780 (5 μM) (or DMSO) plus THP (100 nM). Dead cells were identified based on far red autofluorescence.

(J) Dose-response curves of P cell viability upon THP treatment as in (I). Solid lines represent the best fits of the data to the four-parameter dose-response curve (GraphPad Prism software). EC_{50} [THP] = 17 nM; EC_{50} [THP+BRD4780] = 75 nM. Means ± SD (n = 3 replicates).

See also Figure S4.

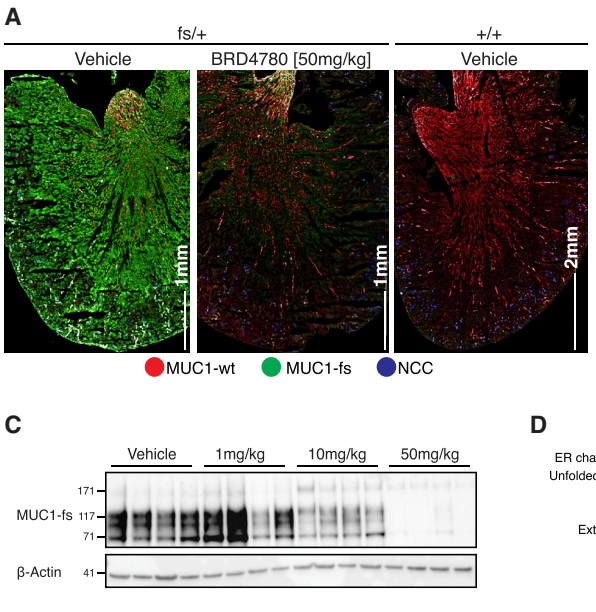

Figure 4. BRD4780 Removes Mutant MUC1-fs from Kidneys of Heterozygous Knockin Mice

(A) IF images of MUC1-fs (green), MUC1-wt (red), and NCC (blue) in fs/+ mice treated for 7 days with vehicle (left) or BRD4780 (50 mg/kg, middle) compared with vehicle-treated +/+ mice (right).

(B) Mean MUC1-fs IF intensity in NCC-positive cells in kidney sections from fs/+ and +/+ mice treated with vehicle or BRD4780 (1, 10, and 50 mg/kg) for 7 days. Mean intensity values were normalized to vehicle-treated +/+ mice (0%) and to vehicle-treated fs/+ mice (100%). Means ± SD (n = 4 mice/genotype/dose). ns, $p > 0.05$; *$p < 0.05$; ***$p < 0.001$.

(C) Immunoblot analysis of MUC1-fs in kidney lysates from fs/+ mice treated with vehicle or BRD4780 (1,10 and 50 mg/kg) for 7 days (n = 4 mice/genotype/dose).

(D) RNA-seq analysis of mouse kidney lysates from fs/+ mice treated with BRD4780 (50 mg/kg/day) or vehicle for 7 days revealed gene ontology (GO) pathways downregulated by BRD4780 (n = 3 mice/genotype).

See also Figure S4.

and mutant proteins, ensuring that only appropriately folded and assembled cargo proteins undergo forward transport through the Golgi apparatus to the endosomal compartment (Gomez-Navarro and Miller, 2016) (Figure 6A). Retrograde transport from the *cis*-Golgi to the ER ensures that immature protein cargoes or escaped ER resident proteins are efficiently transported back to the ER by COPI vesicles (Gomez-Navarro and Miller, 2016) (Figure 6A). However, misfolded proteins can get trapped along the early secretory pathway, between the ER and Golgi compartments (Gomez-Navarro and Miller, 2016). Consistent with this picture, our studies found that MUC1-wt localized clearly and specifically to the plasma membrane in P cells (Figure 1G). In contrast, mutant MUC1-fs was found in a punctate pattern throughout the cytoplasm (Figure 1G). We thus hypothesized that MUC1-fs is trapped somewhere along the early secretory pathway.

To determine exactly where MUC1-fs is retained, we performed a comprehensive co-localization study with markers of different compartments of the secretory pathway (illustration, Figures 6A, 6B, S5A, and S5B). MUC1-fs was substantially more abundant in GM130-positive *cis*-Golgi compartment and TMED9 cargo receptor-positive vesicles than in other compartments (Figures 6A and 6B). TMED9, a member of the p24 cargo receptor family, facilitates packaging and transport between the ER and *cis*-Golgi compartments (Strating and Martens, 2009) and is thought to play a critical role in COPI retrograde transport from the *cis*-Golgi back to the ER (Adolf et al., 2019; Beck et al., 2009). We verified that MUC1-fs co-localized in a vesicular pattern with TMED9 in P cells, as well as in tubular epithelial cells from fs/+ mouse kidneys, from a kidney biopsy of a patient with MKD, and from patient-derived kidney organoids (Figure 6C). Taken together, these data across four different sources (human cells, kidney organoids, kidney biopsy, and mouse kidney) show that MUC1-fs is preferentially co-distributed with the cargo receptor TMED9.

BRD4780 Releases MUC1-fs from the Early Secretory Compartment

To assess the effect of BRD4780 treatment on MUC1-fs subcellular distribution over time, we repeated the co-localization study in the presence of BRD4780 over a 5 h time course (Figure 6D). Compared to baseline (Figure 6B), MUC1-fs was reduced in the early secretory compartment after treatment with BRD4780 and was instead progressively associated with the TGN46-positive trans-Golgi, the EEA1-positive endosomal, and the LAMP1-positive lysosomal compartments (Figure 6D). These results suggested that BRD4780 promotes anterograde trafficking and lysosomal degradation of MUC1-fs by releasing it from the early secretory compartment, where it was trapped in the absence of BRD4780.

An Intact, Functional Secretory Pathway Is Required for BRD4780-Mediated Removal of MUC1-fs

To test whether targeting for lysosomal degradation is the mechanism by which BRD4780 removes mutant MUC1-fs, we disrupted anterograde trafficking and lysosomal degradation before and after treatment with compound. We first blocked vesicular transport between the ER and Golgi with Brefeldin A (BFA) (Chardin and McCormick, 1999). This resulted in the accumulation of an intermediate glycosylated 117 kD MUC1-fs protein in the ER (as compared to 100 kD MUC1-fs protein at baseline; Figures 6E and S5C) (Bosshart et al., 1991). BFA also abrogated the effect of BRD4780 on MUC1-fs clearance (Figure 6E). Second, inhibition of lysosomal degradation by Bafilomycin A (Yoshimori et al., 1991) resulted in a 170 kD MUC1-fs protein retained in late secretory compartments (trans-Golgi, late endosomes, and lysosomes) (Figures 6E and S5C). This 170 kD MUC1-fs protein was present but less abundant in control P cells at baseline, likely representing a fully O-glycosylated version of the protein (Apostolopoulos et al., 2015). Most importantly, lysosomal inhibition with Bafilomycin A prevented BRD4780 from clearing mutant

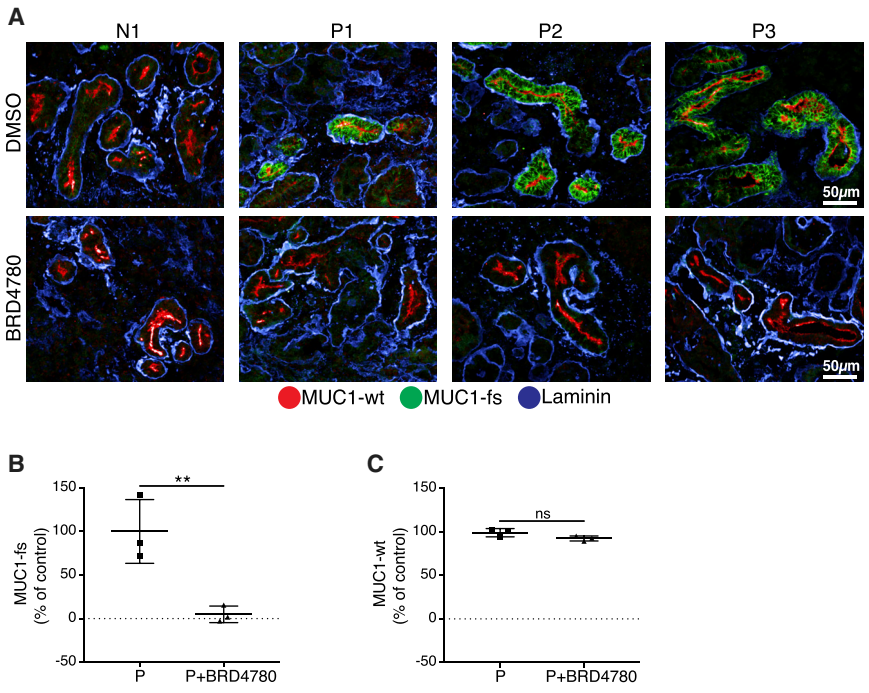

Figure 5. BRD4780 Removes Mutant MUC1-fs from Human iPSC-Derived Kidney Organoids

(A) IF images of MUC1-wt (red), MUC1-fs (green), and laminin (blue) in representative iPSC-derived kidney organoids from a normal individual (N1) and from three MKD patients (P1, P2, and P3), each treated for 72 h with DMSO or BRD4780 (10 μM).

(B) Reduction in MUC1-fs protein abundance in patient P1–P3 iPSC-derived kidney organoids after treatment with BRD4780 for 72 h. Mean fluorescence intensity of tubular MUC1-fs normalized to DMSO-treated normal organoids (0%) and to DMSO-treated patient organoids (100%). Means ± SD (n = 3 replicates). **$p < 0.01$.

(C) No effect of BRD4780 treatment on MUC1-wt abundance in human iPSC-derived kidney organoids generated as in F. Mean intensity values were normalized to DMSO treated normal organoids (100%). Means ± SD (n = 3). ns, $p > 0.05$. See also Figure S4.

MUC1-fs (Figure 6E). Given that treatment with BFA or Bafilomycin A alone resulted in accumulation of MUC1-fs, we concluded that trafficking through the secretory pathway to the lysosome is the fundamental mechanism for MUC1-fs degradation in P cells. In support of this, inhibition of the proteasome had no effect on MUC1-fs accumulation at baseline or on its removal by BRD4780, reinforcing the conclusion that MUC1-fs is degraded in the lysosome (and not the proteasome) (Figure S5D). Taken together, these experiments established that the effect of BRD4780 on clearing MUC1-fs requires a functional secretory pathway and lysosomal degradation.

TMED9 Is Highly Abundant in Kidney Cells Expressing MUC1-fs

Since MUC1-fs was found at highest abundance in TMED9- and GM130-positive compartments at baseline (Figure 6B), we explored the abundance of TMED9 and GM130 in tubular epithelial cells. GM130 abundance was comparable between patient iPSC-derived kidney organoids (P1) relative to controls (N1) and was not affected after treatment with BRD4780 (Figure S6A). In contrast, TMED9 abundance was higher in patient-derived organoids (P1), specifically in cells expressing MUC1-fs, compared to controls (N1). BRD4780 treatment not only cleared MUC1-fs but also reduced TMED9 to levels comparable to cells in N1 organoids (Figure 7A). This further supports the functional role of TMED9 in the entrapment of mutant MUC1-fs in the early secretory pathway.

TMED9 Deletion Phenocopies the Effect of BRD4780 on MUC1-fs Removal

To confirm the role of TMED9 in the mechanism of action of BRD4780, we used CRISPR-Cas9 to delete TMED9 from P cells (Figure 7B). Genetic deletion of TMED9 phenocopied the effect of BRD4780 and resulted in the removal of MUC1-fs from P cells as shown by western blot (Figure 7B) and IF (Figures 7C and 7D). Of note, the abundance of β-COP, an integral component of COPI vesicles (Beck et al., 2009), was not affected either by TMED9 deletion or BRD4780 treatment (Figure 7B). Similarly, MUC1-wt abundance and its localization on the plasma membrane were not affected by TMED9 deletion or BRD4780 treatment (Figure S6B). Thus, BRD4780 appears to work in a targeted fashion to remove the mutant protein cargo associated with TMED9 without disrupting the cell's baseline transport machinery.

BRD4780 Directly Binds Its Molecular Target, TMED9

BRD4780 was originally annotated as a selective ligand for the imidazoline-1 receptor (I1R) and studied as a potential central anti-hypertensive therapy. However, due to lack of efficacy as an anti-hypertensive in several animal studies, BRD4780 was never advanced into the clinic (Munk et al., 1996). The protein nischarin has been proposed as a candidate I1R (Nikolic and Agbaba, 2012; Piletz et al., 2000; Zhang and Abdel-Rahman, 2006). We therefore asked whether nischarin is involved in the mechanism of action of BRD4780 in clearing MUC1-fs. Neither RNAi-mediated depletion nor CRISPR-Cas9-mediated deletion of nischarin in P cells had any effect on MUC1-fs protein abundance or on the efficacy of BRD4780 (Figures 7C, 7D, and S6C), ruling out nischarin as a target of the compound. We also tested 17 additional small molecules annotated as I1R ligands and found that none was active in removing MUC1-fs (Figure S6D). Collectively, these findings suggested that the compound works through a molecular mechanism that does not involve nischarin-I1R.

The TMED9 cargo receptor (1) co-localized in the same vesicular compartments as MUC1-fs at baseline, (2) was highly abundant in MUC1-fs-expressing kidney cells in patient-derived

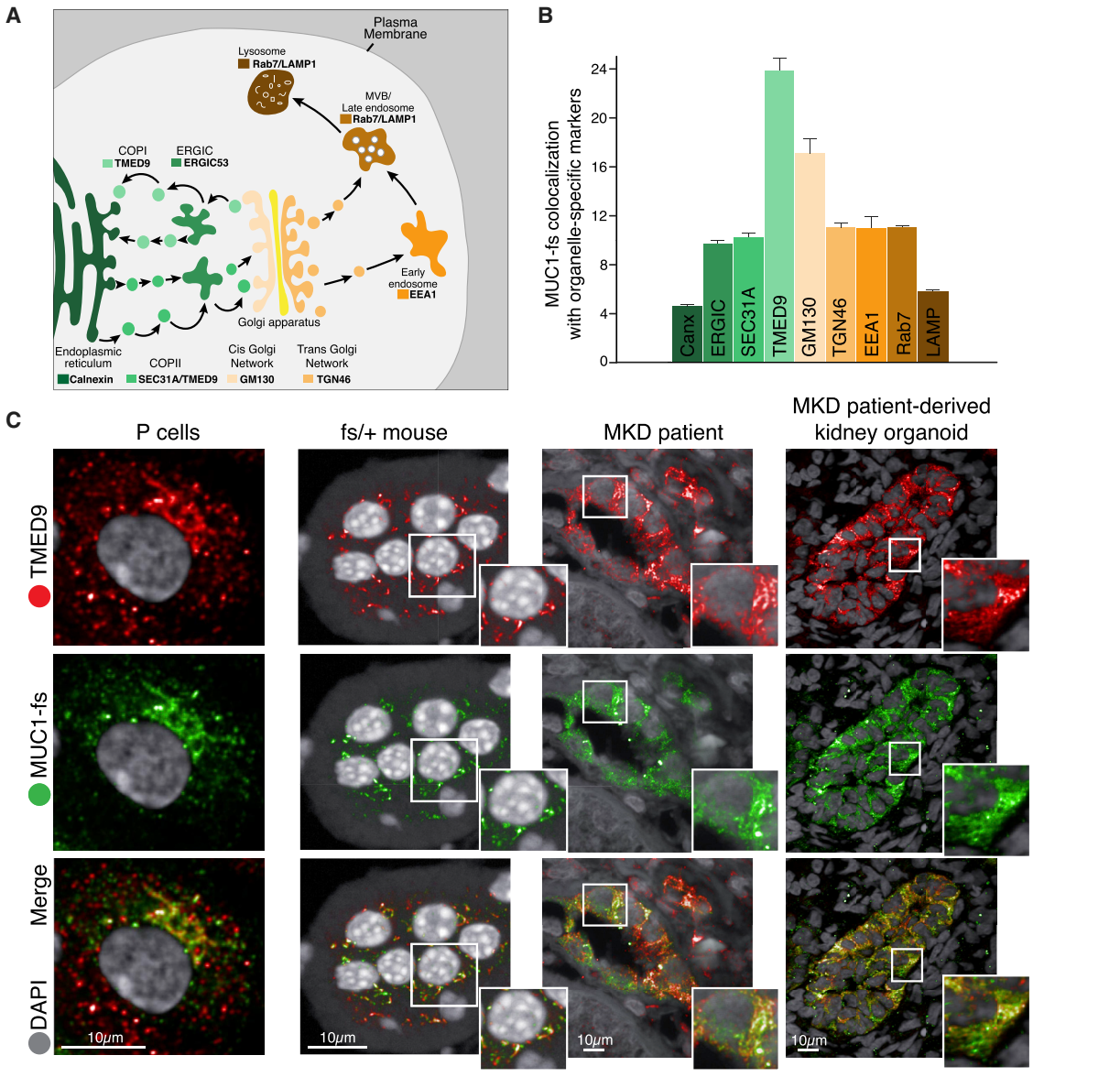

(legend on next page)

organoids, and (3) was reduced to baseline levels after BRD4780 treatment, and (4) its deletion phenocopied the effect of BRD4780. Suspecting that TMED9 might be a molecular target of BRD4780, we sought evidence of direct drug-target engagement. We thus performed a cellular thermal shift assay (CETSA, see STAR Methods) (Jafari et al., 2014; Reinhard et al., 2015), in which unbound proteins denature and precipitate at elevated temperatures, whereas drug-bound proteins remain in solution (Jafari et al., 2014). The CETSA for TMED9 in the presence of BRD4780 demonstrated two findings consistent with direct binding (Figure 7E). First, BRD4780 shifted the TMED9 heat denaturation curve to significantly higher temperatures, and second, BRD4780 also up-shifted the SDS-PAGE migration of TMED9 at all temperatures, consistent with possible covalent modification of TMED9 or other posttranslational modifications (Figure 7E). In contrast, the same experiment for nischarin-I1R revealed no evidence suggestive of direct engagement with BRD4780 (Figure S6E). In aggregate, these studies identified the cargo receptor TMED9 as a molecular target of BRD4780. Furthermore, our data suggested a novel mechanism of action for this compound—namely, that BRD4780 binding to TMED9 releases MUC1-fs from the early secretory compartment, thus promoting its anterograde trafficking into endosomes and finally into lysosomes, where it can be degraded (Figure 7F).

BRD4780 Is Effective in Removing Several Misfolded Proteins

Finally, we explored whether the effect of BRD4780 was specific to the MUC1-fs protein or whether it might also facilitate the removal of misfolded proteins in other proteinopathies involving membrane-associated proteins. We first tested the compound in a cellular model of another autosomal dominant proteinopathy of the kidney, uromodulin (UMOD)-associated kidney disease (Johnson et al., 2017; Schaeffer et al., 2017), a disorder with no available treatment. We applied BRD4780 to AtT20 cells expressing a mutant C126R UMOD protein that accumulates intracellularly. BRD4780 reduced the levels of mutant UMOD protein as measured by IF (Figures S7A and S7B) and confirmed by western blot (Figure S7C).

We also tested whether BRD4780 could alleviate a proteinopathy outside the kidney. Retinitis pigmentosa (RP), the most common inherited retinal degenerative disease, is caused by mutations in rhodopsin (Athanasiou et al., 2018; Dryja and Li, 1995). Most rhodopsin mutations, including P23H, result in a misfolded protein that accumulates intracellularly, leading to photoreceptor cell death (Athanasiou et al., 2018). We applied BRD4780 to N cells overexpressing GFP-tagged rhodopsin P23H and studied the effect of the compound by following GFP fluorescence over 24 h. BRD4780 produced significantly decreased GFP fluorescence at 24 h in GFP-rhodopsin P23H-expressing cells (Figures S7D and S7E). Additionally, the viability of cells expressing mutant rhodopsin significantly improved upon treatment with BRD4780 (Figure S7F).

We then asked whether the effect of BRD4780 was restricted to misfolded proteins whose wild-type versions are membrane-associated (as is the case for MUC1, UMOD, and rhodopsin) (Athanasiou et al., 2018; Hilkens and Buijs, 1988; Johnson et al., 2017; Litvinov and Hilkens, 1993; Schaeffer et al., 2017). We analyzed cells expressing the mutant huntingtin (repeat version) protein, which aggregates in the cytoplasm and the nucleus and causes neuronal toxicity in Huntington's disease (Zoghbi and Orr, 2000). We found that BRD4780 did not reverse or diminish the intracellular accumulation of a GFP-tagged mutant version of huntingtin (97 polyQ) (Figures S7G and S7H).

These findings support the therapeutic potential of BRD4780 for the treatment of toxic proteinopathies caused by mutations in proteins that traffic through the secretory pathway.

DISCUSSION

Treatments are currently lacking for toxic proteinopathies, which affect a wide range of cell types, from neurons to photoreceptors to kidney cells, and result in debilitating and often fatal diseases (Bayer, 2015). New drug development to prevent or halt disease progression has been challenging, due in large part to the dearth of mechanism-based approaches (Dubnikov et al., 2017; Dugger and Dickson, 2017). Here, we elucidate the molecular mechanism underlying a rare and poorly understood autosomal dominant kidney condition, MKD, and show that it is a toxic proteinopathy. Using several models, we showed that MKD is caused by TMED9 cargo receptor-dependent retention of mutant MUC1-fs in the early secretory compartment. We also identified a lead molecule, BRD4780, and demonstrated a novel mechanism of action for the removal of mutant protein, based on binding to TMED9. This study provides answers to several important questions about both MKD and, more generally, mechanisms for clearance of misfolded secretory proteins. It also has important implications for future therapeutic efforts against toxic proteinopathies.

First, our study has elucidated the cellular mechanism by which the toxic proteinopathy MKD begins, with the

Figure 6. MUC1-fs Accumulates in the Early Secretory Pathway, in a TMED9-Positive Compartment

(A) Schematic of the secretory pathway including relevant cellular compartments involved in vesicular transport, color code as labeled.

(B) Subcellular distribution of MUC1-fs in P cells as detected by MUC1-fs co-localization with organelle-specific markers calnexin (Canx, ER), SEC31A (COPII), ERGIC-53 (ERGIC), TMED9 (COPI/II), GM130 (*cis*-Golgi), TGN46, (trans-Golgi), EEA1 (early endosomes), Rab7 (late endosomes), and LAMP1 (lysosomes). Representative images, see Figure S5B. Means ± SD (n = 3 replicates).

(C) Representative IF images showing co-localization of MUC1-fs (green) with TMED9 (red) in four systems: P cells, fs/+ mouse kidney sections, kidney section of MKD patient, and patient iPSC-derived kidney organoids. DAPI, gray.

(D) Change in subcellular distribution of MUC1-fs in P cells after 3 and 5 h of BRD4780 treatment (5 μM). Changes are shown as percentage of DMSO control (shown in B) (n = 3 replicates).

(E) Immunoblot analysis of MUC1-fs in P cells following 24 h inhibition of anterograde ER-Golgi transport by BFA (200 ng/mL) or inhibition of lysosomal degradation by Bafilomycin A (100 nM) in the absence or presence of BRD4780 (5 μM). Both perturbations abolished the BRD4780 effect (n = 3 replicates). See also Figure S5.

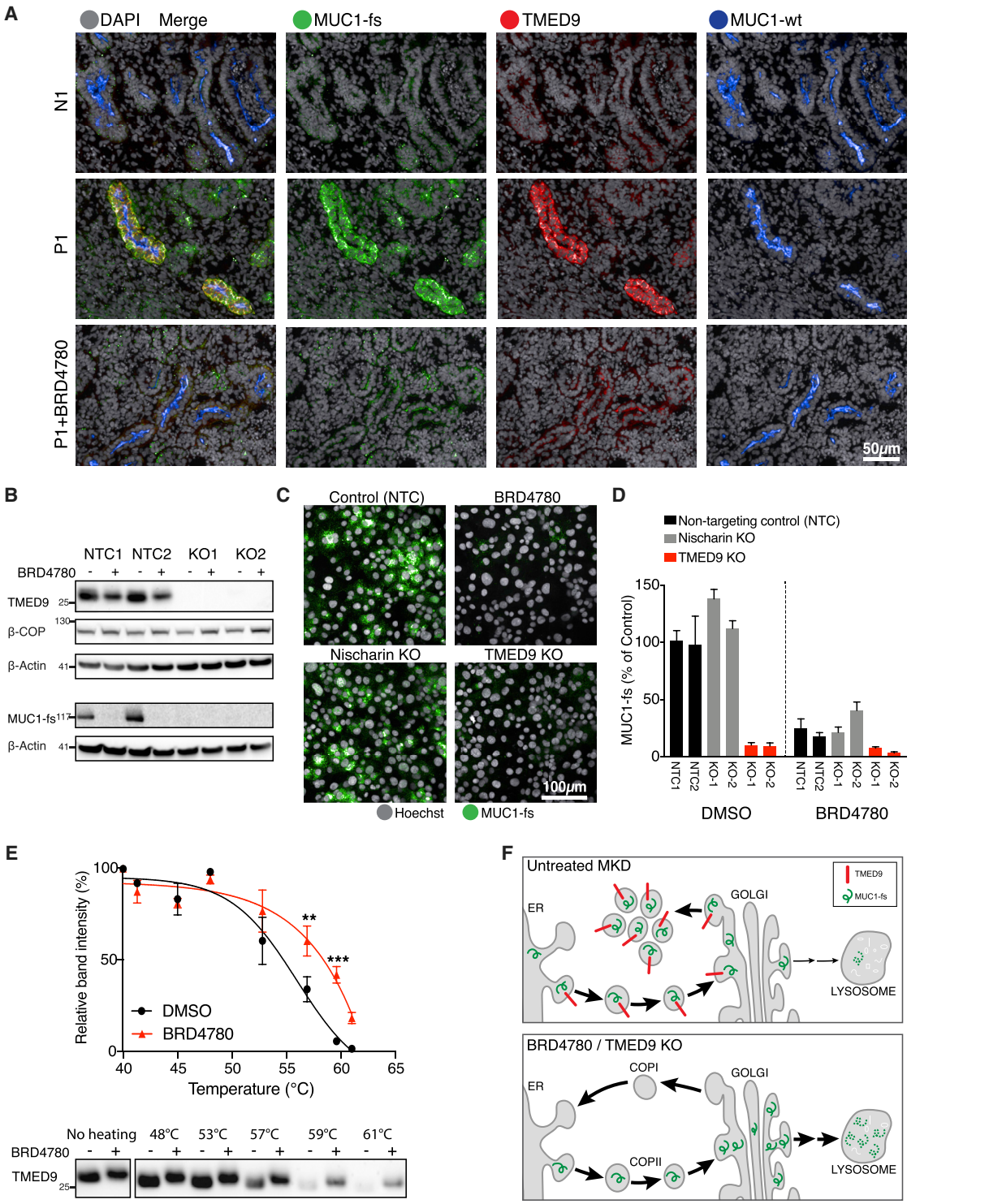

Figure 7. Mechanism of Action of BRD4780 by Engagement of TMED9

(A) IF images of MUC1-fs (green), TMED9 (red), and MUC1-wt (blue), showing increased abundance of TMED9 in MUC1-fs-positive tubules in patient iPSC-derived kidney organoids (middle) compared to normal control (top). TMED9 increased abundance directly correlated with the increase of MUC1-fs and reversed by BRD4780 (10 μM; 72 h).

(B) Immunoblot analysis in TMED9 knockout P cells using two different single guide RNAs (sgRNAs) (KO1, KO2). Non-targeting sgRNAs as controls (NTC1, NTC2). BRD4780 (5 μM) treatment applied for 72 h. Abundance of TMED9, MUC1-fs, and the coatomer protein β-COP as shown.

(legend continued on next page)

accumulation of a mutant neo-protein. Our results show that accumulation of the protein alone is not immediately toxic, owing to the activation of the cytoprotective ATF6 branch of the UPR, and that additional stress signaling likely activates the proapoptotic branches of the UPR, ultimately leading to epithelial cell injury. This may explain the late onset of kidney failure in MKD patients (Bleyer et al., 2017), which is mirrored by the late onset of histologic changes in the kidneys of heterozygous knockin mice. We speculate that while MKD patients accumulate MUC1-fs in kidney tubular epithelial cells throughout life, additional insults (such as exposure to nephrotoxins, inflammation, or infections) and the general decline in UPR homeostasis that accompanies aging (Klaips et al., 2017) may ultimately lead to kidney failure.

In addition to revealing the molecular mechanism of MKD, our studies led to the identification of a lead compound, BRD4780, that may clear not only MUC1-fs but also other misfolded proteins such as UMOD (C126R) and rhodopsin (P23H). In contrast, BRD4780 had no effect on mutant huntingtin, which accumulates in the cytoplasm and nucleus. This underscores the specificity of BRD4780 for misfolded proteins retained in the early secretory pathway. We estimate that more than 20 known proteinopathies are associated with misfolded proteins trapped in compartments between the ER and Golgi apparatus (Dubnikov et al., 2017; Dugger and Dickson, 2017). Thus, BRD4780 may be a therapeutic lead for multiple proteinopathies associated with mutant protein accumulation.

Most importantly, we discovered that the cargo receptor TMED9 (also known as p25 and p24α2 [Gomez-Navarro and Miller, 2016]) is a molecular target for BRD4780, thus uncovering a previously unknown cell biological mechanism for misfolded protein cargo entrapment. Cargo receptors are proteins that span the membrane and physically link cargo with vesicle coat subunits to efficiently and selectively recruit soluble proteins to the emerging vesicles (Barlowe and Helenius, 2016; Geva and Schuldiner, 2014). The mammalian TMED cargo receptor protein family consists of ten members with similar domain architecture (Strating and Martens, 2009). Here, we showed that MUC1-fs, trapped in TMED9 cargo receptor-enriched vesicles between the *cis*-Golgi and the ER, was released by the action of BRD4780 and was thus allowed to traffic through the secretory pathway into endosomes and finally into lysosomes, where it could be degraded. Precisely how BRD4780 binding to TMED9 results in the re-routing of MUC1-fs into the lysosome remains unclear. If TMED9 receptors directly bind MUC1-fs cargo, we can speculate that BRD4780 may work by blocking (either competitively or non-competitively) MUC1-fs binding to its TMED9 receptor. Alternatively, BRD4780 may block TMED9 interactions with other coatomer or integral vesicular proteins, thus indirectly promoting MUC1-fs anterograde trafficking. Future studies will address the detailed molecular interactions between BRD4780, TMED9, and MUC1-fs (or other misfolded protein cargoes) in the early secretory pathway. More generally, our work here has revealed a new strategy of identifying cargo receptors that retain misfolded secretory proteins and finding compounds that promote their anterograde trafficking to the lysosome as a therapeutic approach to toxic proteinopathies.

BRD4780 is a promising therapeutic lead. While careful toxicology studies will be needed, there are several pieces of evidence that are reassuring about the safety of the compound: (1) in *in vitro* studies, BRD4780 showed no overt toxicity at any concentration tested, and in fact, it rescued cells from THP-induced cell death; and (2) in *in vivo* experiments, BRD4780 was well tolerated at several doses up to 50 mg/kg with no overt toxicity. Additionally, BRD4780 has drug-like properties including excellent solubility, good microsomal and plasma stability, low protein binding, and excellent oral bioavailability (Table S2). Therefore, this lead compound holds significant potential for its successful development into a therapy.

In summary, we have elucidated the molecular mechanism underlying MKD and discovered a small molecule with exciting and promising potential as a therapeutic lead for a class of difficult-to-treat diseases with no available treatments. More studies will be required to evaluate the effects of the compound and possible toxicities, as well as the range of additional, currently untreatable, toxic proteinopathies in which it may provide therapeutic benefit.

STAR★METHODS

Detailed methods are provided in the online version of this paper and include the following:

- KEY RESOURCES TABLE
- LEAD CONTACT AND MATERIALS AVAILABILITY
- EXPERIMENTAL MODEL AND SUBJECT DETAILS
  - Human kidney biopsies
  - hMUC1 knock-in mice
  - Cell lines
- METHOD DETAILS
  - Plasmid design and construction
  - Generation of kidney epithelial cells
  - Generation of kidney organoids
  - MUC1 KI replacement mice

(C) IF images of MUC1-fs (green) and Hoechst (gray) in P cells after TMED9 or Nischarin deletion compared to cells treated with non-targeting sgRNA control (NTC) before and after treatment with BRD4780 (5 μM) for 72 h.

(D) Mean MUC1-fs IF intensity in P cells treated as in (C). TMED9 deletion (red) phenocopied the BRD4780 effect. Means ± SD (n > 3 replicates).

(E) Increased thermal stability assessed by CETSA suggestive of direct binding of BRD4780 to TMED9. Representative immunoblot (top) and densitometric analysis (bottom) of TMED9 abundance in P cells at escalating temperatures (as indicated) with or without treatment with BRD4780 (5 μM; 1 h). Higher abundance of TMED9 is noted at temperatures >47°C in the presence of BRD4780. Solid lines represent the best fit of the data to the Boltzmann sigmoid. Means ± SEM (n = 3 replicates). **p < 0.01; ***p < 0.001.

(F) Schematic of proposed BRD4780 mechanism of action illustrating the untreated tubular epithelial cell (top) with MUC1-fs trapped in the early secretory pathway (in TMED9-enriched compartments). Following either engagement of TMED9 by BRD4780 or TMED9 deletion (bottom), MUC1-fs is released from COPI-*cis*-Golgi-COPII compartments, thus allowing its anterograde transport through the secretory pathway to lysosomal degradation.

See also Figures S6 and S7 and Table S2.

- Pharmacokinetics study
- Plasma creatinine measurement
- Mouse transcardial perfusion
- Lentivirus production
- RNA interference
- CRISPR Cas9 system
- Lentivirus transduction
- Transient Transfection
- Stable transfection
- Live cell imaging
- Immunofluorescence staining
- Fluorescence image acquisition
- Fluorescence image analysis
- High content screening
- Kidney histology
- Western Blot and SDS-PAGE Gel Electrophoresis
- Cellular Thermal Shift Assay
- RNA extraction
- XBP1 splicing analysis
- Illumina sequencing
- UPR branch activation
- BRD4780 efficacy experiments
- Evaluation of BRD4780 properties

● QUANTIFICATION AND STATISTICAL ANALYSIS
- RNA-Seq analysis
- Statistical analysis

● DATA AND CODE AVAILABILITY

SUPPLEMENTAL INFORMATION

Supplemental Information can be found online at https://doi.org/10.1016/j.cell.2019.07.002.

ACKNOWLEDGMENTS

We thank Michael E. Cheetham for providing P23H-GFP opsin plasmid, Xueyin Wen for providing cells for huntingtin aggregation experiments and Steven Finkbeiner for providing the original plasmids used to make the HTT 97Q-GFP stable cell line, Kendrah Kidd for assistance with MKD patient samples, Patrick McCarren for assistance with computational chemistry, Jean Santos for technical support with HCS automation, and David Devila and Leslie Gaffney for assistance with graphics. We thank Katherine Blakeslee, Alice McElhinney, Dorothy Pazin, Jennifer T. Chen, and Marisa Cortes for their partnership in the administrative management of this project. We are grateful to all the patients who have generously partnered with us to make this study possible. The patient kidney cell line (P cells) was generated with informed consent under WFUHS IRB00014033, and the patient iPSC lines were generated with informed consent under WFUHS IRB00000352. All RNA-seq data files are deposited at GEO (GEO: GSE129971). This work was funded by a Broad–Israeli Science Foundation Fellowship (M.D.-L.); and the Slim Initiative for Genomic Medicine in the Americas (SIGMA), a collaboration of the Broad Institute with the Carlos Slim Foundation.

AUTHOR CONTRIBUTIONS

M.D.-L., M.K.-A., and A. Greka designed the research; M.D.-L., M.K.-A., M.E., E.-H.S., A.R., N.S., J.R., R.T., G.P., M.S.M., J.G., M.R., E.E., A. Gnirke, M.M., K.H., N.W., J.C.-H.H., M.Z., V.B., S. Kota, and J.S. performed the experiments; M.D.-L., M.K.-A., E.K., A.R.C., F.W., and A.W. performed data analysis; M.D.-L., M.K.-A., E.S.L. and A. Greka wrote the manuscript. A. Greka supervised the project; all authors read and approved the manuscript.

DECLARATION OF INTERESTS

There is a pending United States Patent Application related to this work entitled "Agents for Reversing Toxic Proteinopathies."

Received: August 6, 2018
Revised: April 19, 2019
Accepted: June 28, 2019
Published: July 25, 2019

REFERENCES

Adamson, B., Norman, T.M., Jost, M., Cho, M.Y., Nunez, J.K., Chen, Y., Villalta, J.E., Gilbert, L.A., Horlbeck, M.A., Hein, M.Y., et al. (2016). A Multiplexed Single-Cell CRISPR Screening Platform Enables Systematic Dissection of the Unfolded Protein Response. Cell *167*, 1867–1882.e21.

Adolf, F., Rhiel, M., Hessling, B., Gao, Q., Hellwig, A., Béthune, J., and Wieland, F.T. (2019). Proteomic Profiling of Mammalian COPII and COPI Vesicles. Cell Rep. *26*, 250–265.e5.

Al-Bataineh, M.M., Kinlough, C.L., Poland, P.A., Pastor-Soler, N.M., Sutton, T.A., Mang, H.E., Bastacky, S.I., Gendler, S.J., Madsen, C.S., Singh, S., et al. (2016). Muc1 enhances the β-catenin protective pathway during ischemia-reperfusion injury. Am. J. Physiol. Renal Physiol. *310*, F569–F579.

Apostolopoulos, V., Stojanovska, L., and Gargosky, S.E. (2015). MUC1 (CD227): a multi-tasked molecule. Cell. Mol. Life Sci. *72*, 4475–4500.

Athanasiou, D., Aguila, M., Bellingham, J., Li, W., McCulley, C., Reeves, P.J., and Cheetham, M.E. (2018). The molecular and cellular basis of rhodopsin retinitis pigmentosa reveals potential strategies for therapy. Prog. Retin. Eye Res. *62*, 1–23.

Barlowe, C., and Helenius, A. (2016). Cargo Capture and Bulk Flow in the Early Secretory Pathway. Annu. Rev. Cell Dev. Biol. *32*, 197–222.

Bayer, T.A. (2015). Proteinopathies, a core concept for understanding and ultimately treating degenerative disorders? Eur. Neuropsychopharmacol. *25*, 713–724.

Beck, R., Rawet, M., Wieland, F.T., and Cassel, D. (2009). The COPI system: molecular mechanisms and function. FEBS Lett. *583*, 2701–2709.

Bittker, J.A. (2012). High-Throughput RT-PCR for small-molecule screening assays. Curr Protoc Chem Biol. *4*, 49–63.

Bleyer, A.J., Kidd, K., Živná, M., and Kmoch, S. (2017). Autosomal Dominant Tubulointerstitial Kidney Disease. Adv. Chronic Kidney Dis. *24*, 86–93.

Bosshart, H., Straehl, P., Berger, B., and Berger, E.G. (1991). Brefeldin A induces endoplasmic reticulum-associated O-glycosylation of galactosyltransferase. J. Cell. Physiol. *147*, 149–156.

Brandizzi, F., and Barlowe, C. (2013). Organization of the ER-Golgi interface for membrane traffic control. Nat. Rev. Mol. Cell Biol. *14*, 382–392.

Chardin, P., and McCormick, F. (1999). Brefeldin A: the advantage of being uncompetitive. Cell *97*, 153–155.

Corsello, S.M., Bittker, J.A., Liu, Z., Gould, J., McCarren, P., Hirschman, J.E., Johnston, S.E., Vrcic, A., Wong, B., Khan, M., et al. (2017). The Drug Repurposing Hub: a next-generation drug library and information resource. Nat. Med. *23*, 405–408.

Dryja, T., and Li, T. (1995). Molecular genetics of retinitis pigmentosa. Hum. Mol. Genet *4*, 1739–1743.

Dubnikov, T., Ben-Gedalya, T., and Cohen, E. (2017). Protein quality control in health and disease. Cold Spring Harb. Perspect. Biol. *9*, a023523.

Dugger, B.N., and Dickson, D.W. (2017). Pathology of neurodegenerative diseases. Cold Spring Harb. Perspect. Biol. *9*, a028035.

Geva, Y., and Schuldiner, M. (2014). The back and forth of cargo exit from the endoplasmic reticulum. Curr. Biol. *24*, R130–R136.

Gibier, J.-B., Hémon, B., Fanchon, M., Gaudelot, K., Pottier, N., Ringot, B., Van Seuningen, I., Glowacki, F., Cauffiez, C., Blum, D., et al. (2017). Dual role of MUC1 mucin in kidney ischemia-reperfusion injury: Nephroprotector in early

phase, but pro-fibrotic in late phase. Biochim Biophys Acta Mol Basis Dis *1863*, 1336–1349.

Godiska, R., Mead, D., Dhodda, V., Wu, C., Hochstein, R., Karsi, A., Usdin, K., Entezam, A., and Ravin, N. (2010). Linear plasmid vector for cloning of repetitive or unstable sequences in Escherichia coli. Nucleic Acids Res. *38*, e88.

Gomez-Navarro, N., and Miller, E. (2016). Protein sorting at the ER-Golgi interface. J. Cell Biol. *215*, 769–778.

Hattrup, C.L., and Gendler, S.J. (2008). Structure and function of the cell surface (tethered) mucins. Annu. Rev. Physiol. *70*, 431–457.

Hetz, C. (2012). The unfolded protein response: controlling cell fate decisions under ER stress and beyond. Nat. Rev. Mol. Cell Biol. *13*, 89–102.

Hetz, C., Chevet, E., and Oakes, S.A. (2015). Proteostasis control by the unfolded protein response. Nat. Cell Biol. *17*, 829–838.

Hilkens, J., and Buijs, F. (1988). Biosynthesis of MAM-6, an epithelial sialomucin. Evidence for involvement of a rare proteolytic cleavage step in the endoplasmic reticulum. J. Biol. Chem. *263*, 4215–4222.

Ishikawa, Y., Fedeles, S., Marlier, A., Zhang, C., Gallagher, A.-R., Lee, A.-H., and Somlo, S. (2019). Spliced XBP1 Rescues Renal Interstitial Inflammation Due to Loss of *Sec63* in Collecting Ducts. J. Am. Soc. Nephrol. *30*, 443–459.

Jafari, R., Almqvist, H., Axelsson, H., Ignatushchenko, M., Lundbäck, T., Nordlund, P., and Martinez Molina, D. (2014). The cellular thermal shift assay for evaluating drug target interactions in cells. Nat. Protoc. *9*, 2100–2122.

Johnson, B.G., Dang, L.T., Marsh, G., Roach, A.M., Levine, Z.G., Monti, A., Reyon, D., Feigenbaum, L., and Duffield, J.S. (2017). Uromodulin p.Cys147Trp mutation drives kidney disease by activating ER stress and apoptosis. J. Clin. Invest. *127*, 3954–3969.

Kirby, A., Gnirke, A., Jaffe, D.B., Barešová, V., Pochet, N., Blumenstiel, B., Ye, C., Aird, D., Stevens, C., Robinson, J.T., et al. (2013). Mutations causing medullary cystic kidney disease type 1 lie in a large VNTR in MUC1 missed by massively parallel sequencing. Nat. Genet. *45*, 299–303.

Klaips, C.L., Jayaraj, G.G., and Hartl, F.U. (2017). Pathways of cellular proteostasis in aging and disease. J Cell Biol *217*, 51–63.

Leroy, X., Copin, M.-C., Devisme, L., Buisine, M.-P., Aubert, J.-P., Gosselin, B., and Porchet, N. (2002). Expression of human mucin genes in normal kidney and renal cell carcinoma. Histopathology *40*, 450–457.

Lin, J.H., Li, H., Yasumura, D., Cohen, H.R., Zhang, C., Panning, B., Shokat, K.M., Lavail, M.M., and Walter, P. (2007). IRE1 signaling affects cell fate during the unfolded protein response. Science *318*, 944–949.

Litvinov, S.V., and Hilkens, J. (1993). The epithelial sialomucin, episialin, is sialylated during recycling. J. Biol. Chem. *268*, 21364–21371.

Morizane, R., and Bonventre, J.V. (2017). Generation of nephron progenitor cells and kidney organoids from human pluripotent stem cells. Nat. Protoc. *12*, 195–207.

Munk, S.A., Lai, R.K., Burke, J.E., Arasasingham, P.N., Kharlamb, A.B., Manlapaz, C.A., Padillo, E.U., Wijono, M.K., Hasson, D.W., Wheeler, L.A., and Garst, M.E. (1996). Synthesis and pharmacologic evaluation of 2-endo-amino-3-exo-isopropylbicyclo[2.2.1]heptane: a potent imidazoline1 receptor specific agent. J. Med. Chem. *39*, 1193–1195.

Nath, S., and Mukherjee, P. (2014). MUC1: A multifaceted oncoprotein with a key role in cancer progression. Trends Mol. Med. *20*, 332–342.

Nikolic, K., and Agbaba, D. (2012). Imidazoline antihypertensive drugs: selective i(1) -imidazoline receptors activation. Cardiovasc. Ther. *30*, 209–216.

Piletz, J.E., Ivanov, T.R., Sharp, J.D., Ernsberger, P., Chang, C.H., Pickard, R.T., Gold, G., Roth, B., Zhu, H., Jones, J.C., et al. (2000). Imidazoline receptor antisera-selected (IRAS) cDNA: cloning and characterization. DNA Cell Biol. *19*, 319–329.

Plate, L., and Wiseman, R.L. (2017). Regulating Secretory Proteostasis through the Unfolded Protein Response: From Function to Therapy. Trends Cell Biol. *27*, 722–737.

Reinhard, F.B.M., Eberhard, D., Werner, T., Franken, H., Childs, D., Doce, C., Savitski, M.F., Huber, W., Bantscheff, M., Savitski, M.M., and Drewes, G. (2015). Thermal proteome profiling monitors ligand interactions with cellular membrane proteins. Nat. Methods *12*, 1129–1131.

Remondelli, P., and Renna, M. (2017). The Endoplasmic Reticulum Unfolded Protein Response in Neurodegenerative Disorders and Its Potential Therapeutic Significance. Front. Mol. Neurosci. *10*, 187.

Schaeffer, C., Merella, S., Pasqualetto, E., Lazarevic, D., and Rampoldi, L. (2017). Mutant uromodulin expression leads to altered homeostasis of the endoplasmic reticulum and activates the unfolded protein response. PLoS ONE *12*, e0175970.

Strating, J.R.P.M., and Martens, G.J.M. (2009). The p24 family and selective transport processes at the ER-Golgi interface. Biol. Cell *101*, 495–509.

Subramanian, A., Sidhom, E.-H., Emani, M., Sahakian, N., Vernon, K., Zhou, Y., Kost-Alimova, M., Weins, A., Slyper, M., Waldman, J., et al. (2019). Kidney organoid reproducibility across multiple human iPSC lines and diminished off target cells after transplantation revealed by single cell transcriptomics. bioRxiv. https://doi.org/10.1101/516807.

Takasato, M., Er, P.X., Chiu, H.S., and Little, M.H. (2016). Generation of kidney organoids from human pluripotent stem cells. Nat. Protoc. *11*, 1681–1692.

Walker, B.J., Abeel, T., Shea, T., Priest, M., Abouelliel, A., Sakthikumar, S., Cuomo, C.A., Zeng, Q., Wortman, J., Young, S.K., and Earl, A.M. (2014). Pilon: an integrated tool for comprehensive microbial variant detection and genome assembly improvement. PLoS ONE *9*, e112963.

Walter, P., and Ron, D. (2011). The unfolded protein response: from stress pathway to homeostatic regulation. Science *334*, 1081–1086.

Wenzel, A., Altmueller, J., Ekici, A.B., Popp, B., Stueber, K., Thiele, H., Pannes, A., Staubach, S., Salido, E., Nuernberg, P., et al. (2018). Single molecule real time sequencing in ADTKD-MUC1 allows complete assembly of the VNTR and exact positioning of causative mutations. Sci. Rep. *8*, 4170.

Witkos, T.M., and Lowe, M. (2017). Recognition and tethering of transport vesicles at the Golgi apparatus. Curr. Opin. Cell Biol. *47*, 16–23.

Yamamoto, S., Kaimori, J.-Y., Yoshimura, T., Namba, T., Imai, A., Kobayashi, K., Imamura, R., Ichimaru, N., Kato, K., Nakaya, A., et al. (2017). Analysis of an ADTKD family with a novel frameshift mutation in MUC1 reveals characteristic features of mutant MUC1 protein. Nephrol. Dial. Transplant. *32*, 2010–2017.

Yoshimori, T., Yamamoto, A., Moriyamas, Y., Futais, M., and Tashiroq, Y. (1991). THE JOURNAL OF BIOLOGICAL CHEMISTRY Bafilomycin AI, a Specific Inhibitor of Vacuolar-type H+-ATPase (Inhibits Acidification and Protein Degradation in Lysosomes of Cultured Cells).

Yu, S.M.-W., Bleyer, A.J., Anis, K., Herlitz, L., Živná, M., Hůlková, H., Markowitz, G.S., and Jim, B. (2018). Autosomal Dominant Tubulointerstitial Kidney Disease Due to MUC1 Mutation. Am. J. Kidney Dis. *71*, 495–500.

Zhang, J., and Abdel-Rahman, A.A. (2006). Nischarin as a functional imidazoline (I1) receptor. FEBS Lett. *580*, 3070–3074.

Živná, M., Kidd, K., Přistoupilová, A., Barešová, V., DeFelice, M., Blumenstiel, B., Harden, M., Conlon, P., Lavin, P., Connaughton, D.M., et al. (2018). Noninvasive Immunohistochemical Diagnosis and Novel MUC1 Mutations Causing Autosomal Dominant Tubulointerstitial Kidney Disease. J. Am. Soc. Nephrol. *29*, 2418–2431.

Zoghbi, H.Y., and Orr, H.T. (2000). Glutamine repeats and neurodegeneration. Annu. Rev. Neurosci. *23*, 217–247.

STAR★METHODS

KEY RESOURCES TABLE

REAGENT or RESOURCE	SOURCE	IDENTIFIER
Antibodies		
Fab-A-V5H monoclonal anti-fsMUC1	BioRad	ID: AbD22655.4
Mouse monoclonal anti-MUC1 (Clone 214D4)	StemCell Technologies, Inc.	Cat#: 60137; RRID: AB_1118530
Mouse polyclonal anti-GM130	Abcam	Cat#: ab169276
Rabbit polyclonal anti-TMED9	Proteintech	Cat#: 21620-1-AP; RRID: AB_10858623
Rabbit polyclonal anti-SEC31A	Proteintech	Cat#: 17913-1-AP; RRID: AB_2186378
Rabbit monoclonal anti-EEA1 (C45B10)	Cell Signaling Technologies	Cat#: 3288S; RRID: AB_2096811
Rabbit polyclonal anti-ERGIC-53	Sigma Aldrich	Cat#: E1031; RRID: AB_532237
Mouse monoclonal anti-LAMP1 (D4O1S)	Cell Signaling Technologies	Cat#: 15665; RRID: AB_2798750
Rabbit polyclonal anti-Calnexin	Abcam	Cat#: ab22595; RRID: AB_2069006
Rabbit monoclonal anti-GM130 (D6B1) XP	Cell Signaling Technologies	Cat#: 12480; RRID: AB_2797933
Rabbit monoclonal anti- TNG46	Abcam	Cat#: ab50595; RRID: AB_2203289
Rabbit monoclonal anti-Rab7 (D95F2) XP	Cell Signaling Technologies	Cat#: 9367; RRID: AB_1904103
Rabbit monoclonal anti-Rab11 (D4F5) XP	Cell Signaling Technologies	Cat#: 5589; RRID: AB_10693925
Mouse monoclonal anti-MUC1 (214D4)	Millipore	Cat#05-652-KC; RRID: AB_309877
Armenian monoclonal hamster anti-MUC1	Abcam	Cat#: ab80952; RRID: AB_1640314
Rat monoclonal anti-E Cadherin [DECMA-1]	Abcam	Cat#: ab11512; RRID: AB_298118
Rabbit polyclonal anti-Laminin	Sigma Aldrich	Cat#: L9393; RRID: AB_477163
Rabbit monoclonal Na/K-ATPase	Abcam	Cat#: ab76020; RRID: AB_1310695
Fluorescein labeled Lotus Tetragonolobus Lectin (LTL)	Vector Laboratories	Cat#: FL-1321; RRID: AB_2336559
Rabbit polyclonal anti-Aquaporin 2	Alomone Labs	Cat#: AQP-002; RRID: AB_2039728
Rabbit polyclonal anti-NCC	StressMarq	Cat#: SPC-402; RRID: AB_10641430
Rabbit Monoclonal anti-ERp72	Cell Signaling Technologies	Cat#: 5033; RRID: AB_2165201
Mouse monoclonal anti-Epithelial Membrane Antigen (EMA)	Agilent	Cat#: M061329-2; RRID: AB_2750907
Bacterial and Virus Strains		
sgRNA for TMED9 KO1	Broad Institute GPP	BRDN0003481199
sgRNA for TMED9 KO2	Broad Institute GPP	BRDN0003481863
sgRNA for nischarin KO1	Broad Institute GPP	BRDN0001486234
sgRNA for nischarin KO2	Broad Institute GPP	BRDN0001482682
sgRNA Non-targeting control #1	Broad Institute GPP	BRDN0001148129
sgRNA Non-targeting control #2	Broad Institute GPP	BRDN0001146004
Chemicals, Peptides, and Recombinant Proteins		
BRD4780 (AGN 192403 hydrochloride)	Tocris	Cat#: 1072
PF-429242	Sigma Aldrich	SML0667; CAS: 947303-87-9 (free base)
GSK2656157	Sigma Aldrich	5046510001; CAS: 1337532-29-2
4μ8C	Axon Medchem	1902; CAS: 4003-96-4
Thapsigargin	Sigma Aldrich	T9033; CAS: 67526-95-8
Bafilomycin A	Sigma Aldrich	B1793; CAS: 88899-55-2
Brefeldin A	Sigma Aldrich	B7651; CAS: 20350-15-6
Critical Commercial Assays		
CTS CytoTune-iPS 2.1 Sendai Reprogramming Kit	Thermo Fisher Scientific	A34546
BigEasy v2.0 Linear Cloning Vector pJazz-OK	Lucigen	43036
DeadEnd™ Fluorometric TUNEL System	Promega	G3250

(*Continued on next page*)

Continued

REAGENT or RESOURCE	SOURCE	IDENTIFIER
Deposited Data		
Raw and analyzed data	This paper	GEO: GSE129971; https://www.ncbi.nlm.nih.gov/geo/query/acc.cgi?acc=GSE129971
Experimental Models: Cell Lines		
Human: Normal and MKD patient derived iPSC line	HSCI Core Facility, this paper	N/A
Human: HEK293T	ATCC	CRL-1573; RRID: CVCL_0045
Human: N kidney epithelial cells	This paper	N/A
Human: P kidney epithelial cells	This paper	N/A
Mouse: AtT-20 pituitary cells	ATCC	CCL-89; RRID: CVCL_2300
Experimental Models: Organisms/Strains		
Mouse: wt/+ knock-in:129S2	GenOway, this paper	N/A
Mouse: fs/+ knock-in: 129S2	GenOway, this paper	N/A
Oligonucleotides		
Primer: MUC1 Forward: GGCAGAGAAAGGAAAT GGCACATCACT	This paper	N/A
Primer: MUC1 Reverse: CTGCTGCTCCTCACAG TGCTTACAGGT	This paper	N/A
Primer: XBP1 Forward: TTACGAGAGAAAACTCATGGCC	This paper	N/A
Primer: XBP1 Reverse: GGGTCCAAGTTGTCCAGAATGC	This paper	N/A
Recombinant DNA		
Plasmid: P23H mutant-GFP rhodopsin	Gift from Michael E. Cheetham Laboratory	N/A
Plasmid: GFP huntingtin 97Q	Gift from Steven Finkbeiner Laboratory	N/A
Plasmid: Nischarin KD hairpin shRNA construct	Broad Institute GPP	TRCN0000256843
Plasmid: Empty vector for shRNA control	Broad Institute GPP	TRCN0000208001
Software and Algorithms		
Harmony High-Content Imaging and Analysis Software	Perkin Elmer	HH17000001
GraphPad Prism: Version 7	GraphPad	graphpad.com
RStudio: Version 1.0.153	RStudio	rstudio.com
Other		
Opera Phenix High-Content Screening System	Perkin Elmer	HH14000000

LEAD CONTACT AND MATERIALS AVAILABILITY

Further information and requests for resources and reagents should be directed to and will be fulfilled by the Lead Contact, Anna Greka (agreka@broadinstitute.org). Plasmids generated in this study are available by contacting the Lead Author with no restrictions. Cell lines generated in this study are available by contacting the Lead Author with no restrictions. Mouse lines generated in this study are available by contacting the Lead Author with no restrictions.

EXPERIMENTAL MODEL AND SUBJECT DETAILS

Human kidney biopsies

Kidney tissue was obtained as discarded tissue from surgical nephrectomies performed for clinical indications. Control samples were examined by a renal pathologist to select tissue for further processing. For MKD patient tissue, samples from kidney cortex and medulla were collected from a 50-year-old female patient with advanced disease undergoing nephrectomy for a suspicious cyst that was proven benign. Biopsies were obtained with informed consent under WFUHS IRB00014033.

hMUC1 knock-in mice

wt/+ and fs/+ knock-in (KI) 129S2 mice were generated by GenOway (Lyon, France) using embryonic stem (ES) cells genetically modified by homologous recombination, by knocking in the human *MUC1* gene (including the promoter region) into the murine *MUC1* locus. Mice were maintained on a 12 h light/dark cycle at 18–26°C in an AAALAC accredited facility and fed *ad libitum* with water and PicoLab® Rodent Diet 20 pellets (LabDiet). Both male and female mice ranging in age from 4 – 24 months were used for experimentation. All animal experiments were approved by the Institutional Animal Care and Use Committee (IACUC) at The Broad Institute of MIT and Harvard and were conducted in accordance with National Institutes of Health (NIH) animal research guidelines.

Cell lines

iPS cell lines from three MKD patients (P1, female; P2, female; P3, male) and their unaffected siblings (N1, female; N2, male; N3, male) were derived from erythroblasts using CTS CytoTune-iPS 2.1 Sendai Reprogramming Kit (Thermo Fisher Scientific) at the Harvard Stem Cell Institute iPS Core Facility. Cell lines were characterized for pluripotency and spontaneous differentiation to the three germ layers using qPCR based on standard protocols at the HSCI Core Facility. All iPSC cultures were maintained at 37°C with 5% CO2 in mTeSR1 medium in T25 flasks coated with Matrigel. Cells were passaged using Gentle Cell Dissociation Reagent. All lines were confirmed to be karyotype normal and maintained below passage 15. All iPSC lines were generated with informed consent under WFUHS IRB00000352.

HEK293T cells (ATCC) were cultured according to standard protocol at 37°C with 5% CO2 in Dulbecco's Modified Eagle's Medium (DMEM) supplemented with 10% Fetal Calf Serum (Life Technologies), 100 units/mL penicillin and 100 μg/mL streptomycin (Life Technologies).

N and P (female) immortalized kidney epithelial cells, generated in this study, were maintained at 37°C with 5% CO2 in RenaLife Renal Basal Medium supplemented with RenaLife LifeFactors® (Lifeline Cell Technology), with the exclusion of Gentamycin and Amphotericin B. For all experiments, P cells were maintained below passage 12. The cells were generated with informed consent under WFUHS IRB00014033.

AtT-20 mouse pituitary cells (ATCC) stably transfected with cDNAs encoding WT-UMOD or UMOD mutant C126R were maintained at 37°C with 5% CO2 in DMEM:Nutrient Mixture F-12 (DMEM/F12) (Thermo Fisher Scientific) supplemented with 10% Fetal Calf Serum (Life Technologies), 100 units/mL penicillin and 100 μg/mL streptomycin (Life Technologies) and 0.8 mg/mL of G418 (Sigma-Aldrich).

All cell lines were routinely checked and were negative for mycoplasma. Where applicable, cell lines were sequenced for authentication according to ATCC guidelines.

METHOD DETAILS

Plasmid design and construction

Plasmid constructs for *in vivo* expression of MUC1-wt and MUC1-fs proteins were based on the normal and mutant *MUC1* alleles of MKD patient F6:IV-3, each containing a VNTR region comprising 37 near-identical 60-mer repeat units that had been completely sequenced and assembled previously (Kirby et al., 2013). The frameshift mutation is found in the second repeat unit of this allele. The *MUC1* tandem array and flanking regions were PCR-amplified in 50 μl containing 50 ng genomic DNA, 15 pmol forward (GGCA GAGAAAGGAAATGGCACATCACT) and 15 pmol reverse primer (CTGCTGCTCCTCACAGTGCTTACAGGT), 0.2 mM of each dNTP and 1.25 U PrimeSTAR GXL DNA Polymerase in 1x PrimeSTAR GXL Premix (Takara). The thermoprofile was 1 min at 94°C, 22 cycles of 10 s at 98°C, 10 s at 65°C, 6 min at 68°C, with final extension for 10 min at 68°C. Bona fide full-length PCR products spanning chr1:155,160,024-155,162,601 of the incomplete hg19 reference genome (4.15 kb in F6:IV-3) were gel-purified, cleaned up by QiaQuick gel-extraction kits (QIAGEN) and TOPO-TA cloned in pCR-4-TOPO vector in TOP10 cells (Thermo Fisher Scientific). Transformants were Sanger sequenced with vector and insert primers to determine the frameshift mutation status and to screen out clones harboring PCR induced non-synonymous mutations within reach of unique sequencing primers, i.e., flanking the 1.3 kb inaccessible core of the tandem repeat. Clones passing this test were then subjected to full-length Pacific Biosciences sequencing of a 4.7 kb fragment generated by digestion with NspI and PvuI. The clone chosen for MUC1-fs expression constructs included a synonymous PCR-induced mutation of a leucine codon located 731 codons downstream of the codon altered by the frameshift mutation.

To replace one copy of the endogenous mouse *Muc1* gene with WT and mutant alleles of the human *MUC1* gene, including its regulatory sequences, the 3.9 kb DraIII fragment was subcloned into an acceptor vector providing sequences upstream and downstream sequences of hg19 chr1:155157737-155165183 which contains the *MUC1* gene body, the promoter and enhancer region up to and including micro RNA gene MIR92B, as well as flanking restriction sites required for the generation and analysis of KI transgenic mice generated by GenOway (Lyon, France). Before assembling the constructs, two synonymous single-base changes were introduced to the normal *MUC1* sequence. Both artificial markers disrupt a restriction site and thus provide a simple genotyping assay for tracking and identification purposes. Marker 1 is a G to A substitution at hg19 chr1:155,161,995, which disrupts a BseY1 site in a PCR product generated with primers GCTACCACAGCCCCTAAACC and GCTGTGGCTGGAGAGTACG. Marker 2 is a T to A substitution at hg19 chr1: 155,160,802, which disrupts a KpnI site in a PCR product generated with primers CCAGCCATAGCACCAAGACT and GGAAGGAAAGGCCGATACTC. The modified VNTR-containing WT clone was verified by full-length Pacific Biosciences sequencing

as before. *MUC1* transgene fragments were assembled in the BigEasy v2.0 linear cloning vector pJazz-OK (Lucigen), which reduces torsional stress during replication and helps maintain otherwise unstable and difficult-to-clone sequences (Godiska et al., 2010). The final constructs underwent three independent sequence-validation checks: i) Illumina Mi-Seq sequencing with paired-end 150 base reads and pilon analysis (Walker et al., 2014) that detected errors in the vector sequence and none in the cloned insert but has blind spots in the tandem repeat region, ii) full-length Pacific Biosciences sequencing of the 3.9-kb DraIII fragment excised from the linear pJazz clones, and iii) subcloning of the 3.9-kb DraIII in a low-copy number pSMART LC-Kan vector (Lucigen), followed by transposon hopping for deep bidirectional Sanger sequencing and tandem-repeat assembly. This sequence validation employed the same approach that was used for the original identification of the frameshift mutation in MKD patients (Kirby et al., 2013). The final constructs (22 kb including the vector) were provided to GenOway for KI transgenesis and development of a mouse model for MKD.

Wild-type *UMOD* mRNA was reverse-transcribed from human total kidney RNA, PCR amplified, and cloned into a pCR3.1 vector (Thermo Fisher Scientific). Constructs were introduced into E. *coli* TOP 10'F strain (Thermo Fisher Scientific), and candidate recombinant clones were confirmed by sequencing. Mutant UMOD construct c.385T>C (C126R-*UMOD*) was prepared by site-directed mutagenesis of the *WT-UMOD*/pCR3.1 construct.

P23H mutant-GFP rhodopsin plasmid in pEGFP-N1 vector was kindly provided by Michael E. Cheetham.

Plasmid of huntingtin gene exon 1 fragments containing 97 CAG (97Q) repeats fused to GFP was kindly provided by Steven Finkbeiner.

Generation of kidney epithelial cells

Kidney tissues from control and MKD patient were finely minced, digested with 1 mg/mL Collagenase- type II (Worthington Corp) at 37°C for 30 min and passed through a series of sieves (100 μm, 70 μm). Tubules that were retained on the top of 70 μm sieve were plated in RenaLife Epithelial Medium on collagen coated plates for propagation. Next, cells were immortalized using lentivirus carrying human Telomerase Reverse Transcritpase (hTERT) produced in HEK293T cells. Briefly, viral supernatant was added to cells in the presence of 1 μg/mL Polybrene. Cells were then spun at 500 g for 1 h at 30°C, then washed with DMEM/F12 (Thermo Fisher Scientific) and incubated in RenaLife Epithelial Medium for 24 h, followed by a second identical cycle of viral transduction. Transduced cells were selected and expanded in 100 μg/mL of Hygromycin B (Thermo Fisher Scientific), then cloned by serial dilution. Clones of control (N) cells and MKD patient (P) cells were selected for MUC1 protein abundance and cell polarization on Corning Transwell® Semipermeable support plates (Thermo Fisher Scientific).

Generation of kidney organoids

Kidney organoids were generated from iPS cells derived from MKD patients and their unaffected siblings. iPS cells were seeded at 375,000 cells per T25 flask in mTeSR1 media (Stem Cell Technologies) supplemented with 10 μM/mL Rock Inhibitor Y-27632 (72304, Stem Cell technologies). After 24 h, cells were treated with 8 μM CHIR 99021 (R&D Systems) in STEMdiff APEL2 Medium (05270, Stem cell Technologies) for 4 days, followed by addition of 200 ng/mL Recombinant Human FGF-9 (100-23, Peprotech) and 1 μg/mL heparin (Sigma-Aldrich) for 3 more days. At day 7, cells were dissociated into single cells using ACCUTASE (Stem Cell Technologies) at 37°C for 5 min. Then, 500,000 cells were pelleted at 350 x *g* for 2 min (twice with 180° flip after first spin) and transferred onto a transwell membrane (Corning). Pellets were incubated with 5 μM CHIR 99021 in STEMdiff APEL2 Medium for 1 h. Afterward, 200 ng/mL Recombinant Human FGF-9 and heparin were added for 5 days, followed by 2 days incubation with 1 μg/mL heparin. For the following 15 days, organoids were kept in STEMdiff APEL2 Medium. Media were changed every other day.

MUC1 KI replacement mice

The wt/+ and fs/+ KI replacement mice were developed by GenOway (Lyon, France) using human *MUC1-wt* and *MUC1-fs* constructs described above. The *MUC1* constructs were knocked into ES cells using homologous recombination. ES cells were injected into blastocysts, and chimeric 129S2 mice were generated. Following breeding, heterozygous mice expressing either hMUC1-wt or hMUC1-fs were obtained.

Mouse genotyping was performed by Transnetyx, using real-time PCR to identify mice expressing the human *MUC1* versus the mouse *MUC1* version.

Pharmacokinetics study

The pharmacokinetics study for BRD4780 was performed by WuXi AppTec (Hong Kong) in fasted 129S2 male mice. A single dose (10, 20 or 50 mg/kg) of BRD4780 was orally administered and the concentrations of the compound were analyzed in mice plasma and kidney homogenate using LC-MS/MS for up to 24 h.

Plasma creatinine measurement

Monthly blood samples from conscious mice were collected into lithium heparin with plasma separator tubes (BD Microtainer) by 4 mm lancet puncture of the submandibular vein (World Precision Instruments), alternating right and left sides. Samples were centrifuged at 2000 x g at 4°C for 10 min, with transfer of plasma to an Eppendorf DNA LoBind Microcentrifuge Tube followed by another centrifugation at 2000 x g 2000 for 10 min at 4°C. Plasma samples were kept at −80°C until sent for creatinine measurement to UAB Biochemical Genetics Laboratory, University of Alabama.

Mouse transcardial perfusion

Transcardial perfusion-fixation was performed for testing MUC1-fs colocalization with TMED9-positive vesicles. Mice were anesthetized with 3 L/min of 3% isoflurane in O_2 for 5 min (Combi-vet® system; Rothacher Medical, Bern, Switzerland). Anesthetized mice were transcardially perfused with 0.1 M PBS (pH 7.4) followed by 4% PFA in 0.1 M PBS. Kidneys were removed, transected into halves and postfixed in 4% PFA for 2 h at 4°C. Fixed tissue was rinsed in 0.1 M PBS, then cryoprotected 1 h with 10% sucrose, 5 h with 20% sucrose, and overnight in 30% sucrose. Cryoprotected tissue was mounted in OCT in a dry ice-ethanol bath and processed for IF studies.

Lentivirus production

Lentiviral stocks were generated by transfection of HEK293T cells. Cells were transfected with the lentiviral target vector together with a 2nd generation packaging plasmid containing gag, pol and rev genes (e.g., pCMV-dR8.91), and a VSV-G expressing plasmid using TransIT-LT1 transfection reagent (Mirus Bio) as recommended by the manufacturer. Lentiviral supernatants were collected at 48 h and 72 h post transfection, then were passed through a 0.45 mm filter and applied directly to cells or aliquoted and frozen.

RNA interference

For knockdown of nischarin (putative I1R), a short hairpin RNA (shRNA) plasmid construct (TRCN0000256843) was used to generate lentiviral stocks. For empty vector (EV) control, a similar plasmid lacking the nischarin shRNA was used (TRCN0000208001). P cells were transduced with either targeting shRNA or EV.

CRISPR Cas9 system

To generate Cas9-expressing P cells, the Cas9 expression vector pXPR_BRD111 was used. For knockout of nischarin, lentiviral stocks expressing single guide RNA (sgRNA) plasmid constructs (BRDN0001486234;KO1, BRDN0001482682;KO2) were used. For TMED9 knockout, lentiviral stocks expressing sgRNA plasmid constructs (BRDN0003481199;KO1, BRDN0003481863;KO2) were used. Non-targeting sgRNAs (BRDN0001148129;NTC1, BRDN0001146004;NTC2) were used as controls. Cas9-expressing P cells were assayed for Cas9 activity using pXPR_BRD047 plasmid which expresses eGFP and an sgRNA targeting eGFP.

Lentivirus transduction

P cells were transduced with either lentiviral stocks of nischarin shRNA or Cas9 expressing vector. Viral supernatants were applied to cells for 24 h in the presence of 4 μg/mL protamine sulfate (194729MP, Biomedicals). Infected cells were washed three times to remove viral particles and transduced cells were selected in either 2 μg/mL puromycin (Thermo Fisher Scientific)(for nischarin shRNA transduction) or 8 μg/mL blasticidin (Thermo Fisher Scientific)(for stable Cas9 expression). For sgRNA transduction, Cas9-expressing P cells were transduced as described above and selection was made using 2 μg/mL puromycin.

Transient Transfection

N cells plated in 96-well plates were transfected with 20 ng/well of P23H mutant rhodopsin-GFP plasmid DNA using Lipofectamine 3000 (Thermo Fisher Scientific). Eight h post- transfection, the cells were washed and processed as described below.

Stable transfection

AtT20 cells at 75% confluence were transfected with 4 μg DNA using Lipofectamine 2000 (Thermo Fisher Scientific). After 72 h, cells were trypsinized, diluted, and selected in 0.8 mg/mL G418 (Thermo Fisher Scientific). UMOD-expressing clones were selected for further study using PCR, DNA sequencing, and western blot analyses.

HEK293T cells were transfected with Huntingtin 97Q repeats fused to GFP and selected in 0.8 mg/mL G418 (Thermo Fisher Scientific).

Live cell imaging

To study apoptosis and cell death in N and P cells, 384 well Cell Carrier Ultra plates (Perkin Elmer), pre-coated with 0.25 mg/mL Synthemax II SC Substrate (Corning) were used. For UPR branch activation experiments, N and P cells were treated as described in the corresponding figure legends. CellEvent Caspase-3/7 Green Detection Reagent (Thermo Fisher Scientific) and DRAQ7 (Biostatus) were used at 1:5000 to monitor apoptosis and cell death respectively. Cells were imaged daily during 4 days to monitor viability and image analysis was performed as describe below. For rescue experiments, P cells were plated on 96 well Cell Carrier Ultra microplates (Perkin Elmer) at 30,000 cells/well and cultured for 24 h. BRD4780 (5 μM) was applied as a pretreatment for 48 h prior to thapsigargin exposure and throughout the experiment. Thapsigargin was applied at increasing doses and the plates were imaged daily thereafter. To monitor cell death in N cells transiently expressing P23H mutant rhodopsin, DRAQ7 (1:5000) was added with DMSO or 5 μM BRD4780 treatments. Treated plates were imaged 30 min post-dye application and daily thereafter.

Immunofluorescence staining

Cells grown on CellCarrier-96 or-384 well Ultra microplates (PerkinElmer) were fixed 10 min in PBS containing 4% PFA (Electron Microscopy Sciences), permeabilized 15 min in 0.5% Triton X-100 (Sigma-Aldrich), blocked for 1 h in blocking reagent (100mM Tris HCL

pH8; 150mM NaCL; 5g/L Blocking Reagent [Roche]) and treated for 1 h with primary antibodies diluted in blocking reagent (1:500, monoclonal Fab-A-V5H anti-fsMUC1, AbD22655.2, Bio-Rad; 1:2000, monoclonal Mouse anti-MUC1 (CD227), StemCell Technologies, Inc.; 1:200, polyclonal Mouse anti-GM130, Abcam; 1:100, polyclonal Rabbit anti-TMED9, Proteintech; 1:800, polyclonal Rabbit anti-SEC31A, Proteintech; 1:400, monoclonal Rabbit anti-EEA1 (C45B10), Cell Signaling Technology; 1:100, polyclonal Rabbit anti-ERGIC-53, Sigma- Aldrich; 1:400, monoclonal Mouse anti-LAMP1 (D4O1S), Cell Signaling Technology; 1:1000, polyclonal Rabbit anti-Calnexin, Abcam; 1:2000, monoclonal Rabbit anti-GM130 (D6B1) XP, Cell Signaling Technology; 1:200, monoclonal Rabbit anti- TNG46, Abcam; 1:100, monoclonal Rabbit anti-Rab7 (D95F2) XP, Cell Signaling Technology; 1:100, monoclonal Rabbit anti-Rab11 (D4F5) XP, Cell Signaling Technology). Fixed, stained cells were washed three times in PBS and incubated for 1 h with secondary antibodies in blocking solution (1:500, Alexa Fluor 488® Goat anti-Mouse IgG, Thermo Fisher Scientific; 1:500, Alexa Fluor 647® F(ab')2-Goat anti-Rabbit IgG, Thermo Fisher Scientific; 1:2000, Hoechst Thermo Fisher Scientific), then washed three times in PBS and imaged.

Kidney organoids were immersion-fixed for 15 min in 4% PFA at 4°C and subsequently frozen in OCT using dry ice and 100% ethanol. Six μm-thick cryostat sections (Leica) were thaw-mounted on microscope slides (Fisherbrand™ Superfrost™ Plus, Fisher Scientific) and kept in the cryostat (at −26°C) for the duration of the sectioning process. Prior to immunostaining, organoid sections were rinsed in PBS for 5 min, incubated for 20 min at room temperature (RT) in PBS blocking solution containing 5% normal donkey serum (EMD Millipore) and 1.5% Tween® 20 (Sigma- Aldrich), then incubated overnight at 4°C with primary antibodies diluted in the same blocking solution (1:500, monoclonal Armenian hamster anti-MUC1, Abcam; 1:500, monoclonal Fab-A-V5H anti-fsMUC1, Bio-Rad; 1:300 monoclonal Rat anti-E Cadherin [DECMA-1], Abcam; 1:500 polyclonal Rabbit anti-Laminin, Sigma-Aldrich; 1:500 monoclonal Rabbit Na/K-ATPase, ab76020, Abcam; 1:300 Fluorescein labeled Lotus Tetragonolobus Lectin (LTL), Vector Laboratories; 1:100, polyclonal Rabbit anti-TMED9, Proteintech). Immunostained organoid sections were then rinsed three times for 10 min in PBS and incubated for 2 h at RT with secondary antibodies diluted in PBS containing 1.5% Tween-20 (1:500, Alexa Fluor® 488-conjugated AffiniPure F(ab')$_2$ Fragment Goat anti-Human IgG, Jackson Immunoresearch; 1:500, Alexa Fluor® 647-conjugated AffiniPure Goat anti-Armenian hamster IgG, Jackson Immunoresearch; 1:1000, Alexa Fluor® 568 Goat anti-Rabbit IgG, Thermo Fisher Scientific; 1:500, DyLight 405 Goat anti-Rat IgG, Jackson Immunoresearch). After a 10 min PBS wash, organoid sections were incubated for 5 min in PBS containing DAPI (1:10000, Thermo Fisher Scientific). The stained organoid sections were then washed three times for 10 min in PBS, air-dried and mounted with ProLong Gold Antifade Mountant (Thermo Fisher Scientific).

Mice were anesthetized with 3 L/min O_2 mixed with 3% isoflurane using the Combi-vet® system (Rothacher Medical, Bern, Switzerland) for 5 min. Mouse kidneys were removed, sagittally cut in half and rapidly frozen in Tissue-Tek® O.C.T. Compound, Sakura® Finetek (OCT) (VWR) using dry ice and 100% ethanol. Five μm-thick sagittal cryosections (Leica) were thaw mounted on microscope slides (Fisherbrand™ Superfrost™ Plus, Fisher Scientific) and kept in the cryostat (at −26°C) for the duration of the sectioning process. Sections were immersion-fixed for 10 min in 4% PFA (Electron Microscopy Sciences), then washed in PBS. The slides were then subjected to antigen retrieval by immersion in 10 mM citric acid buffer (pH = 6), for 10 min at 95°C. Following a wash in PBS, the slides were incubated for 20 min at room temperature in PBS blocking solution containing 5% normal goat serum (Jackson ImmunoResearch), 0.2% Triton X-100 (Sigma-Aldrich) and 2% bovine serum albumin (BSA) (Sigma-Aldrich). Sections were then incubated at 4°C overnight with primary antibodies diluted in the same blocking solution (1:500, monoclonal Armenian hamster anti-MUC1, Abcam; 1:500, monoclonal Fab-A-V5H anti-MUC1-fs, Bio-Rad; 1:400, polyclonal Rabbit anti-Aquaporin 2, Alomone Labs; 1:1000, polyclonal Rabbit anti-NCC, StressMarq; 1:300, monoclonal Rabbit anti-ERp72, Cell Signaling Technology; 1:100, polyclonal, Rabbit anti-TMED9, Proteintech). Stained sections were rinsed three times for 10 min in PBS and incubated with secondary antibodies diluted in PBS containing 0.1% Triton X-100 for 2 h at RT (1:500, Alexa Fluor® 488-conjugated AffiniPure F(ab')$_2$ Fragment Goat anti-Human IgG, Jackson Immunoresearch; 1:500, Alexa Fluor® 647-conjugated AffiniPure Goat anti-Armenian hamster IgG, Jackson Immunoresearch; 1:1000, Alexa Fluor® 568 Goat anti-Rabbit IgG, Thermo Fisher Scientific). Following three washes of 10 min in PBS, stained sections were treated with 1:10000 DAPI solution (Thermo Fisher Scientific) in PBS for 5 min, washed three times for 10 min in PBS, air-dried and mounted using ProLong Gold Antifade Mountant (Thermo Fisher Scientific).

To detect apoptotic nuclei, mouse tissue sections were prepared and fixed as described above, permeabilized for 20 min with 0.2% Triton X-100 (Sigma-Aldrich) and stained using terminal deoxy transferase uridine triphosphate nick-end labeling (TUNEL) technique (Promega), following the manufacturer's protocol. Stained sections were washed and treated with 1:10000 DAPI solution (62248, Thermo Fisher Scientific) in PBS for 5 min. Following three washes of 10 min in PBS, the sections were air-dried and mounted using ProLong Gold Antifade Mountant (Thermo Fisher Scientific).

Human kidney biopsy paraffin sections were deparaffinated, hydrated and subjected to antigen retrieval by immersion in 10 mM citric acid buffer (pH = 6). Endogenous peroxidase was blocked with 1% sodium azide and 0.3% H2O2 for 10 min followed by blocking with 5% fetal bovine serum (FBS) in PBS for 30 min. Sections were then incubated at 4°C overnight with primary antibodies in 5% BSA in PBS (1:500, Alexa Fluor® 488-conjugated anti-MUC1-fs Fab fragment AbD2265454, Bio-Rad; 1:100, monoclonal Mouse anti-Epithelial Membrane Antigen (EMA), Agilent; 1:100, polyclonal Rabbit anti-TMED9, Proteintech). Following washing, the sections were incubated for 1 h at 37°C with secondary antibodies diluted in 5% BSA in PBS (1:500, Alexa Fluor® 555 Donkey anti-Rabbit IgG, Thermo Fisher Scientific; 1:500, Alexa Fluor® 647 Donkey anti-Mouse IgG, Thermo Fisher Scientific). Slides were washed and mounted in ProLong Gold Antifade Mountant with DAPI (Thermo Fischer Scientific).

Fluorescence image acquisition

All fluorescence imaging performed in this study was done using the Opera Phenix High-Content Screening System (PerkinElmer). For fluorescence imaging of cells (live cell or fixed cell imaging), CellCarrier Ultra microplates (96- or 384-well, Perkin Elmer) were used, and a minimum of nine fields was acquired per well using 20x or 63x water immersion objectives in a confocal mode. For kidney organoids and mouse kidney section imaging, microscope slides (Fisherbrand™ Superfrost™ Plus, Fisher Scientific) were used. The entire specimen was first imaged for DAPI at 5X using the PreciScan™ feature (Perkin Elmer) to identify tissue. Pre-identified tissue regions were then imaged at higher resolution (20X or 63x water immersion objectives, confocal mode).

Fluorescence image analysis

Image analysis for all imaging experiments was performed using the Harmony software (PerkinElmer).

Cell nuclei were first identified using Hoechst staining, and cell number was calculated. Cytoplasmic regions were then detected around each nucleus based on combined channels. The cells from the edge of the field were eliminated from the analysis. For the quantification of protein abundance, the total signal intensity value for each antibody was calculated separately in the cell cytoplasm and the average signal per cell was calculated for each well. For quantitation of MUC1-fs cellular distribution and trafficking, the analysis was performed as described in Figure S5A using the ''spot'' identification feature for the detection of MUC1-fs and the different organelles.

For live cell image analysis, caspase 3/7 activation and/or DRAQ7 signal were used to calculate the fraction of cells going through apoptosis and/or cell death, respectively. Single cells were first identified using the digital phase contrast channel and cell number was calculated. Fluorescence intensities were then measured and the threshold for caspase 3/7 and DRAQ7 positive signal was determined. As an output, the fraction of live (neither caspase3/7 nor DRAQ7 signal detected), apoptotic (caspase3/7 positive) or dead cells (DRAQ7 positive) was calculated in each well at a particular time point.

For the measurement of P cell rescue from THP-induced cell death by BRD4780, no dyes were added to avoid any influence on cell growth. Digital phase contrast images were used for cell identification and count, and autofluorescence in the far-red channel was used for detection of dead cells. Cells with no autofluorescence were identified and calculated as live cells.

For the GFP-rhodopsin experiments, cells were identified by digital phase contrast. GFP signal was calculated only in cells expressing GFP signal above a minimal background (to identify successfully transfected cells) and the mean intensity was averaged for each well.

For GFP-Huntingtin experiments, GFP signal in each cell was calculated using the ''spot'' identification feature, and total spot intensity for single cells was calculated and averaged for each well.

For image analysis of mouse kidney sections, MUC1-fs and MUC1-wt mean intensities were calculated in kidney sections of mice treated with either vehicle or BRD4780. As MUC1-fs and MUC1-wt levels varied in different kidney regions, and as sections could contain different portions of kidney regions, the levels of these proteins were systematically analyzed only in NCC-positive distal convoluted tubules. To this end, single cell nuclei were first identified using DAPI channel, followed by cytoplasm detection using all combined channels, excluding the nucleus. Each fluorescent channel intensity was measured and a threshold was set for the identification of NCC positive cells. MUC1-fs and MUC1-wt levels were then calculated only in the NCC positive cells.

For apoptosis detection using TUNEL staining, TUNEL signal was calculated in each nucleus of the section (excluding the tissue periphery) and the threshold for TUNEL-positive cells was established. Total number of apoptotic cells was calculated as the number of nuclei in which TUNEL signal exceeded the threshold level. This number was normalized (divided) to the total number of nuclei in the entire tissue section. For visualization and validation of tissue image analysis, single cells depicted by the analysis were plotted as a scatterplot according to their position on the slide using Spotfire software allowing thus to observe tissue architecture and positioning apoptotic cells within their relative location. The identified TUNEL positive cells were highlighted by a red color.

For image analysis of organoids, tubular structures expressing MUC1 proteins were identified and selected using MUC1-wt positive staining. For sequence analysis illustration, see Figure S4F. First, a reference region was generated according to MUC1-wt positive staining in order to depict the apical part of each tubule. Subsequently, the intratubular region was defined based on the reference region with the addition of 20 μm to expand this region in order to capture the entire tubule. Laminin signal was then used to exclude the extracellular space. Finally, MUC1-fs signal was depicted within this intratubular area using the ''spot'' identification feature, and mean intensity of this signal was averaged for entire organoid section. MUC1-wt signal intensities were calculated within each WT reference region and averaged for the entire section.

High content screening

For high content screening, an automated system was used, consisting of robotic arms; plate stackers; a HighRes Pin Tool; Liconic incubators; Biotek plate washers; dedicated Thermo Fisher Combi Multidrop dispensers for each assay reagent; and PerkinElmer High Content Imaging Instrument Opera Phenix, all choreographed by Cellario software. Cell fixation and immunostaining were all performed in a custom-designed light-protected hood (HighRes Biosolutions). Data analysis and representation was performed using Genedata Screener (Genedata AG) and Spotfire (TIBCO).

For the IF screen, P cells were seeded 24 h prior to compound treatment at a density of 12,000 cells/well in 384 well CellCarrier Ultra plates (Perkin Elmer), pre-coated with 0.25 mg/mL Synthemax II SC Substrate (Corning). Compounds of the repurposing library set (Corsello et al., 2017) were used at 5 doses (35, 3.5, 0.35, 0.035 and 0.0035 μM) for the primary screen and 10 doses (16, 5.6, 1.8, 0.6,

0.21, 0.07, 0.02, 0.008, 0.002 and 0.0008 μM) for the following screens. The compounds, in two replicates, were transferred from compound source plates to the cell plates using the HighRes Pin Tool. DMSO was used as a negative control and JQ1 (250 nM) (a bromodomain inhibitor) was chosen as a positive control, based on earlier studies showing its potent effect on reducing total MUC1 mRNA levels (data not shown). After 48 h incubation, cells were fixed for 20 min in 4% PFA (Electron Microscopy Sciences) in PBS, washed twice, then permeabilized (10 min) with 0.5% Triton X-100 (Sigma-Aldrich) in PBS and washed once more. Cells were blocked for 10 min at RT with Blocking solution (100mM Tris HCL pH8; 150mM NaCL; 5g/L Blocking Reagent [Roche]), then incubated 90 min at RT with one of the following primary antibodies in Roche Blocking solution: 1:500, monoclonal Fab-A-V5H anti-MUC1-fs, Bio-Rad; 1:2000, monoclonal mouse anti-MUC1 (214D4), Millipore; 1:1000, monoclonal, Rabbit anti-GM130 (D6B1) XP, Cell Signaling Technology. The primary antibody cocktail was incubated at RT for 1.5 h, followed by four PBS wash cycles. The secondary antibody cocktail contained four components that were all prepared at a 1:1000 dilution in the Roche blocking solution and consisted of Alexa Fluor® 488-conjugated AffiniPure F(ab')$_2$ Fragment Goat anti-Human IgG, Jackson Immunoresearch; Alexa Fluor® 647-conjugated Goat anti-Rabbit IgG, Thermo Fisher Scientific; Alexa Fluor® 546 Goat anti-mouse IgG, Thermo Fisher Scientific and Hoechst 33342 stain, Thermo Fisher Scientific. The secondary antibody cocktail was incubated at RT for 45 min, followed by four PBS wash cycles. Finally, plates were sealed with a Plate Loc plate and stored in Liconic incubator at 10°C until imaging.

Image acquisition and analysis was done as described in the Fluorescence image acquisition and analysis section. Following image analysis, three parameters were selected, i) MUC1-fs and ii) MUC1-wt total cytoplasm intensity (averaged per cell) and iii) cell number as was detected by Hoechst 33342 stained nuclei. The levels of MUC1-fs and MUC1-wt found following DMSO and JQ1 were defined as 0 and −100% activity, respectively. The values obtained for all other compounds, including BRD4780, were normalized accordingly. Cell number was normalized to DMSO control. All compound concentrations showing > −20% reduction in cell number were masked out. Based on ± 3 median absolute deviation value, hit calling criteria for the primary and secondary screens were chosen as MUC1-fs reduction > 30% in 2 or more consecutive concentrations for both replicates. For the secondary screen, dose response curves were generated for each parameter using Genedata Screener (Genedata AG), and positive hits for the profiling screens were selected based on the compound's activity in reducing MUC1-fs without cell toxicity. MUC1-fs specificity (according to MUC1 fs/wt ratio) was used as an additional positive criterion for selection.

For the RT-PCR-based screen (Bittker, 2012), P cells seeded at 2000 cells/well in 384-well, clear bottom, white wall plates were grown for 24 h, then treated with profiling compounds transferred by pinning to duplicate plates. JQ1 (250 nM) and DMSO were used for controls as above. After 24 h, cells were washed and cDNAs were made using ABI Cells-to-Ct kit (Thermo Fisher Scientific, Waltham, MA). MUC1 and HMBS delta Cp values were determined using a Roche LightCycler 480 Instrument and TaqMan probes for MUC1 FAM (4351368 assay ID Hs00159357_m1) and HMBS VIC (4448486- assay ID Hs00609297_m1) (Thermo Fisher Scientific), in 5 μL reactions. The fold change effect of the compounds on total MUC1 mRNA was normalized to JQ1 and DMSO controls, as described above.

For the viability profiling screen, P cells were seeded 12 h prior to profiling compound treatment at a density of 12,000 cells/well in 384 well Cell Carrier Ultra plates (Perkin Elmer), pre-coated with 0.25 mg/mL Synthemax II SC Substrate (Corning). After 24 h, CellEvent Caspase-3/7 Green Detection Reagent (Thermo Fisher Scientific) and DRAQ7 (Biostatus) were added at 1:5000 final dilution in the presence or absence of thapsigargin (100 nM). Cells were imaged daily during 7 days to monitor viability. Image acquisition and analysis was done as described above and viability was assessed as fraction of live cells at day 5 of thapsigargin treatment, and at the day 6 for DMSO.

Kidney histology

Formalin-fixed, paraffin-embedded kidney sections of 4 μm thickness were stained with periodic acid–Schiff (PAS) by the Harvard Medical School Pathology Core. Light microscopy PAS images were analyzed in a blinded fashion and classified using standard criteria. Immunoperoxidase staining for MUC1-wt and MUC1-fs was performed by standard protocols using anti-MUC1-wt (ab80952, Abcam) and monoclonal Fab-A-V5H anti-MUC1-fs (Bio-Rad). HRP-linked goat anti-Armenian hamster (Thermo Fisher Scientific) was used to detect MUC1-wt and Mouse anti V5-HRP (Thermo Fisher Scientific) was used to detect MUC1-fs.

Western Blot and SDS-PAGE Gel Electrophoresis

Cells were lysed in lysing buffer solution (Cell Signaling Technology) containing protease inhibitors (Roche) and phosphatase inhibitors (Roche). Mouse kidney tissues were lysed by tissue homogenizer (Tissue-Tearor™, BioSpec Products) in lysing buffer solution containing inhibitors as above, followed by 20 min rocking at 4°C and centrifugation at 16,000 g, 4°C for 5 min. To normalize protein concentration, proteins in the supernatant of cells or of kidney lysates were quantified using the Pierce BCA Protein Assay Kit (Thermo Fisher Scientific). Normalized protein lysates were then mixed with NuPAGE LDS sample buffer (Thermo Scientific) and NuPAGE reducing agent (Thermo Scientific) and heated to 75°C for 10 min prior to SDS-PAGE gel electrophoresis using NuPAGE Tris-Acetate SDS Running Buffer (Thermo Scientific) or NuPAGE MES SDS running buffer (Thermo Fisher Scientific) depending on protein molecular weight of interest. Electrophoretically separated proteins were transferred to a nitrocellulose membrane (BioRad) using Trans-Blot® Turbo™ Blotting System (BioRad) following manufacturer's protocol. Membranes were blocked in 5% Nonfat Dry Milk (Cell Signaling Technology) in PBS with 0.1% Tween® 20 (PBS-T), and probed with primary antibody overnight at 4°C. Following three washes with PBS-T, the membranes were incubated with secondary antibody for 1 h at room temperature,

washed three more times in PBS-T, and incubated with Super Signal West Dura (Thermo Fisher Scientific) or Super Signal West Pico (Thermo Fisher Scientific) and immunoreactive bands were imaged by G:BOX Chemi XT4 (G:BOX-CHEMI-XT4, Syngene).

Cellular Thermal Shift Assay

For Cellular Thermal Shift Assays (CETSAs)(Jafari et al., 2014; Reinhard et al., 2015), P cells were treated in the presence or absence of BRD4780 for 1 h, harvested (trypsinized), washed in PBS, resuspended in PBS (containing protease inhibitors) and distributed in 0.2ml PCR tubes (100 μl; 600,000 cells). Cells were incubated at their designated temperatures for 3min, then at 25°C for 3min and lysed by the addition of 1% NP-40. Immediately thereafter, samples were snap frozen and thawed using thermal cycler set at 25°C. Samples were spun at 20'000xg for 20min (4°C) to remove precipitated protein and the supernatant was analyzed by western blot to examine the TMED9/Nischarin thermal stability.

RNA extraction

RNA was extracted from cells seeded onto 12-well plates using the RNeasy kit (QIAGEN), following the manufacturer's protocol. RNA was eluted with Nuclease-Free water and total yield and purity of RNA were assessed by NanoDrop 2000 (Thermo Fisher Scientific).

RNA was extracted from sagittal kidney sections. Kidney tissue was homogenized using tissue homogenizer (Tissue-Tearor™, BioSpec Products) in 1 mL of TRIzol Reagent (Thermo Fisher Scientific). Following 5 min incubation, 0.2 mL chloroform (Sigma-Aldrich) was added, and samples were vigorously mixed for 30 s, then centrifuged at 12,000 x g at 4°C for 15 min. The upper aqueous phase containing RNA was then vigorously mixed with 0.5 mL of isopropanol for 30 s. After 10 min incubation at RT, the samples were centrifuged at 12,000 x g at 4°C for 10 min. The pellet was resuspended in 1 mL of 75% ethanol and centrifuged at 12,000 x g 4°C for 5 min. The RNA pellet was then air-dried for 15 min, dissolved in 50 μL of Nuclease-Free Water (Thermo Fisher Scientific), treated with DNase I, Amplification Grade (Thermo Fisher Scientific) following the manufacturer's protocol and assessed for yield and purity by NanoDrop 2000 (Thermo Fisher Scientific).

XBP1 splicing analysis

XBP1 splicing was analyzed by standard RT-PCR. Briefly, RNA was isolated from patient cells using the RNeasy Mini Kit (QIAGEN). One μg of RNA was converted to cDNA using the SuperScript First-Strand Synthesis system for RT-PCR (Invitrogen). The primer sequences used are as follows: Human XBP1 Forward Primer: 5′ TTA CGA GAG AAA ACT CAT GGC C 3′. Human XBP1 Reverse Primer: 5′ GGG TCC AAG TTG TCC AGA ATG C 3′. PCR was carried out on 3 μL of the resulting cDNA solution using the OneTaq Hot Start Master Mix (NEB). Five μL of PCR product was run on a 2% agarose gel for 90 min at 150 V.

Illumina sequencing

cDNA library construction and Illumina sequencing were performed at the Broad Institute sequencing platform as follows. Concentrations of purified RNA were measured with the Quant-iT™ RiboGreen® RNA Assay Kit (Thermo Fisher Scientific) and normalized to 5 ng/μL. An automated variant of the Illumina TruSeq™ Stranded mRNA Sample Preparation Kit was used for library preparation from a 200 ng aliquot of RNA. This method preserves strand orientation of the RNA transcript and uses oligo dT beads to select mRNA from the total RNA sample. Following cDNA synthesis and enrichment, cDNA libraries were quantified with qPCR using the KAPA Library Quantification Kit for Illumina Sequencing Platforms and then pooled equimolarly. For Illumina sequencing, pooled libraries were normalized to 2 nM and denatured using 0.1 N NaOH prior to sequencing. Flow cell cluster amplification and sequencing were performed according to the manufacturer's protocols using either the HiSeq 2000 or HiSeq 2500. Each run was a 101 bp paired-end with an eight-base index barcode read. Data was analyzed using the Broad Institute Picard Pipeline, which includes de-multiplexing and data aggregation.

UPR branch activation

The involvement of the UPR in MUC1-fs induced cytotoxicity was detected in N and P cells using immunoblot or IF. For IF experiments, N and P cells were plated at 9,000 and 6, 000 cells/well respectively and cultured for 24 h. Cells were pretreated with either DMSO or 10 μM inhibitors of ATF6 (PF-429242, Sigma- Aldrich), PERK (GSK2656157, Sigma- Aldrich) and IRE (4μ8C, Axon Medchem) for 1 h, followed by application of different concentrations of THP. Cell viability was determined using caspase activation as describe above. For immunoblot experiments, N and P cells were grown in 6-well plates to high confluence and treated with DMSO or THP (100 nM) for 12 h. The cells were then processed for immunoblot analysis as described above.

BRD4780 efficacy experiments

The effect of BRD4780 on MUC1-fs levels in mouse kidney was tested in age-matched fs/+ and wt/+ male mice (27-38 weeks old). BRD4780 (1, 10 and 50 mg/Kg/day) or vehicle (PBS) were administered daily by oral gavage for 7 days. Animal weight was observed daily to monitor toxicity. On day 7, mice anesthetized for 5 min with 3 L/min 3% isoflurane in O_2 using the Combi-vet® system (Rothacher Medical, Bern, Switzerland) were sacrificed, and kidneys were removed for further analysis.

The effect of BRD4780 in kidney organoids was tested on Day 25 organoids transferred from Transwell membranes to low-attachment Corning® Costar® TC-Treated 24-Well Plates (Sigma-Aldrich) in 250 μL STEMdiff APEL2 Medium (Stem Cell Technologies). Organoids were treated with 10 μM BRD4780 or DMSO vehicle for 72 h at 37°C. After 72 h, organoids were washed twice with PBS and processed for IF detection.

In P cells, detection of MUC1-fs at baseline and following BRD4780 and secretory pathway perturbations was done using immunoblot and IF analyses. For immunoblots experiments, P cells were grown in 6-well plates to high confluence. For IF experiments, P cells were plated in 384-well plates at 12,000 cells/well. Following 24 h, cells were treated with 5 μM BRD4780 or DMSO alone, or in combination with 100 nM Bafilomycin A (Sigma-Aldrich), or 200ng/mL Brefeldin A (Sigma-Aldrich) for a maximum period of 24 h as indicated. For TMED9 or Nischarin depletion experiments, transduced/transfected P cells were plated either in 96-well plates at 60,000 cells/well for IF, or grown in 6-well plates to high confluence for immunoblot detection. Cells were then treated with 5 μM BRD4780 or DMSO for 24 h (for IF detection) or 72 h (for immunoblot analysis) and were processed accordingly. AtT-20 cells stably transduced with C126R mutant UMOD plasmid were treated for 72 h with 10 μM of BRD4780 or vehicle DMSO. For thapsigargin treatment, AtT-20 cells pretreated 24 h with 1 or 10 μM of BRD4780 were exposed to 10 nM of thapsigargin for 48 h. The cells were either imaged for IF detection of UMOD or processed for immunoblot analysis. N cells transiently expressing P23H-GFP mutant rhodopsin were plated in 96-well plates at 20,000 cells/well and grown for 24 h, then DMSO or 5 μM BRD4780 were added to the medium as a pre-treatment. Following 48 h, cells in the presence or absence of BRD4780, were transfected with P23H mutant rhodopsin-GFP plasmid. Eight h post- transfection, the cells were washed once and media containing DMSO or 5 μM BRD4780 was added. Plates were imaged 24 h following transfection.

HEK293T stably expressing huntingtin 97Q-GFP were treated with 10 μM of BRD4780 or vehicle DMSO, then monitored for GFP intensity by live cell imaging.

For RNA-Seq experiments to determine cellular effect of BRD4780, N and P cells were plated in 12-well plates at 200,000 cells/well. Subsequently, 1 μM of BRD4780 or DMSO were applied for 24 h followed by 12 h exposure to 100 nM of thapsigargin (THP) or DMSO for control. At the end of the experiment, RNA was extracted from treated cells and sequencing was performed.

Evaluation of BRD4780 properties

Compound solubility was determined in PBS at pH 7.4. Each compound was prepared in triplicate at 500 μM in both 100% DMSO and 100% PBS by drying down 10 μL of a 10 mM DMSO compound stock solution and then adding 200 μL of PBS. Compounds were allowed to equilibrate at room temperature with a 750 rpm vortex shake for 18 h. Prior to equilibration, StirStix were added to each well to aid in the prevention of aggregation. After equilibration, samples were centrifuged (32 x g) to remove undissolved particulates and a 20 μL aliquot of supernatant was diluted with 480 μL acetonitrile. The resulting solution was analyzed by UPLC-MS/MS with compounds detected by SIR detection on a single quadrupole mass spectrometer. The peak areas of the 100% DMSO samples were used to create a two-point calibration curve to which the peak area response in PBS was fit. Solubility in PBS was calculated using the following equation: Conc. (PBS) = Conc. (DMSO) x [area (PBS)/area (DMSO)]. (LC System, Waters Acquity H-Class; MS System, Waters Acquity SQ Detector; Column, Waters Acquity UPLC BEH C18, 1.7 μm, 1.0x50 mm; Mobile Phase A, Water with 0.1% Ammonium Hydroxide (or 0.5% trifluoroacetic acid); Mobile Phase B, Acetonitrile with 0.1% Ammonium Hydroxide (or 0.6% trifluoroacetic acid); Flow Rate, 0.45 mL/min; Column Temperature, 60°C)

Plasma stability was determined at 37°C at 5 h in plasma. Each compound was prepared in duplicate at 5 μM in plasma diluted 50/50 (v/v) with PBS pH 7.4 (0.95% acetonitrile, 0.05% DMSO). Duplicate plates were prepared. One plate was incubated at 37°C for 5 h with a 350 rpm orbital shake, while the other plate was immediately quenched. Each well was quenched by adding acetonitrile to a 3:1 ratio (v/v, ACN/plasma). After quenching, samples were centrifuged (32 x G) to pellet precipitated particulates and an aliquot of supernatant was diluted 50/50 (v/v) with water. The resulting solution was analyzed by UPLC-MS/MS with compounds detected by MRM detection on a triple quadrupole mass spectrometer. The compound peak areas at 0 and 5 h were compared to determine a percent remaining. Percent remaining in plasma was calculated through the following equation: % remaining = [area (5 h)/area (0 h)] x 100. (LC System, Waters Acquity I-Class; MS System, AB Sciex Triple Quad 4500; Column, Waters Acquity UPLC BEH C18, 1.7 μm, 2.1x50 mm; Mobile Phase A, Water with 0.1% formic acid; Mobile Phase B, Acetonitrile with 0.1% formic acid; Flow Rate, 0.90 mL/min; Column Temperature, 55°C)

Plasma protein binding was determined by equilibrium dialysis using the Rapid Equilibrium Dialysis (RED) device (Pierce Biotechnology). Each compound was prepared in duplicate at 5 μM in plasma (0.95% acetonitrile, 0.05% DMSO) and added to one side of the membrane with PBS pH 7.4 added to the other side. Compounds were incubated at 37°C for 5 h with a 350 rpm orbital shake. After incubation, an aliquot was taken from each side of the membrane and quenched by adding acetontrile to a 3:1 ratio (v/v, ACN:plasma). After quenching, samples were centrifuged (32 x g) to pellet precipitated particulates and an aliquot of supernatant was diluted 50/50 (v/v) with water. The resulting solution was analyzed by UPLC-MS/MS with compounds detected by MRM detection on a triple quadrupole mass spectrometer. The compound peak area on the buffer side of the membrane was compared to the peak area on the plasma side of the membrane to determine percent bound. Percent bound in plasma was calculated through the following equations: % free = [area (buffer)/area (plasma)] x 100. % bound = 100 - % free. (LC System, Waters Acquity I-Class; MS System, AB Sciex Triple Quad 4500; Column, Waters Acquity UPLC BEH C18, 1.7 μm, 2.1x50 mm; Mobile Phase A, Water with 0.1% formic acid; Mobile Phase B, Acetonitrile with 0.1% formic acid; Flow Rate, 0.90 mL/min; Column Temperature, 55°C)

Compound stability was determined at 37°C at 1 h in liver microsomes. Each compound was prepared in duplicate at 1 μM in liver microsomes diluted 50/50 (v/v) with PBS pH 7.4. After addition of compounds to microsome mixture, the plate was sealed and vortexed and 100μL of each sample was added to 300μL acetonitrile (with internal standard). Assay plate was incubated at 37°C for 1 h with a 350 rpm orbital shake, and following the h 100μL of each sample was added to 300μL acetonitrile (with internal standard). After quenching, samples were refrigerated for at least 1 h. The samples were centrifuged (32 x g) to pellet precipitated particulates and an aliquot of supernatant was diluted 50/50 (v/v) with water. The resulting solution was analyzed by UPLC-MS/MS with compounds detected by MRM detection on a triple quadrupole mass spectrometer. The compound peak areas in the 0 and 1 h samples, -NADPH sample, and no compound control sample were compared to determine a percent remaining. Percent remaining in microsomes was calculated through the following equation: % remaining = [area (1 h)/area (0 h)] x 100. (LC System, Waters Acquity I-Class; MS System, AB Sciex Triple Quad 4500; Column, Waters Acquity UPLC BEH C18, 1.7 μm, 2.1x50 mm; Mobile Phase A, Water with 0.1% formic acid; Mobile Phase B, Acetonitrile with 0.1% formic acid; Flow Rate, 0.90 mL/min; Column Temperature, 55°C)

QUANTIFICATION AND STATISTICAL ANALYSIS

RNA-Seq analysis

Data processing and statistical analysis for all RNA-Seq experiments was performed in RStudio – Version 1.0.153 as follows. First, bam files obtained from the Broad Institute sequencing platform were reverted to FASTQ files followed by alignment of paired end reads to the mm10 mouse or hg19 human reference genome using STAR. Quality control metrics were obtained using RNA-SeQC and expression levels were estimated by running RSEM with default parameters on these alignments. RSEM's gene level expression estimates were normalized according to edgeR for sequencing depth and multiplied by 1,000,000 to obtain counts per million (CPM). Genes with CPM < 1 in fewer than three samples (number of replicates) were removed from further analysis. TMM normalization was applied to the data, accounting for gene composition. For further downstream analysis (e.g., boxplots) the data was log2-transformed. In mouse kidney RNA-Seq experiments, two samples were removed from the analysis (fs/+ treated with BRD4780 replicate 3 and +/+ treated with BRD4780 replicate 1) due to significantly low library sizes. For statistical testing, generalized linear models obtained in edgeR were applied with the assumption of negative binomial distribution with default parameters using the expected counts from RSEM followed by likelihood ratio test. Genes were considered to be significantly differentially expressed using a significance level of $\alpha = 0.05$ following Benjamini Hochberg correction for multiple hypothesis testing.

The Functional Annotation Tool DAVID was used to detect significant signatures differentially downregulated in fs/+ mice following BRD4780 treatment. Differentially downregulated genes were analyzed using GO terms of Biological Processes. The reported p value is a modified Fisher Exact p value (EASE score) and a gene set was considered enriched if a significance level of $\alpha = 0.05$ was reached following Benjamini Hochberg correction.

UPR branch activation analysis is presented as boxplots. Each box of the boxplot consists of genes comprising an individual UPR branch (Adamson et al., 2016). The expression of each gene in the group is plotted as mean of the scaled expression profiles obtained from three replicates.

Statistical analysis

Statistical analysis was performed and presented using Graphpad Prism version 7.0 software. All data are presented as means ± standard deviation unless otherwise specified in the figure legends. The exact value of 'n' for each experiment can be found in the figure legends. Statistical comparisons of two groups for a single variable with normal distributions were analyzed by unpaired t test. Statistical comparisons of two or more groups with one independent variable were analyzed by One-way ANOVA with Tukey post-tests. Statistical comparisons of two or more groups with two independent variables were analyzed by Two-way ANOVA with Tukey post-tests. *p < 0.05 **p < 0.01 ***p < 0.001 ****p < 0.0001

DATA AND CODE AVAILABILITY

The accession number for the RNA-Seq data reported in this paper is GEO: GSE129971.

The published article includes all datasets generated or analyzed during this study.

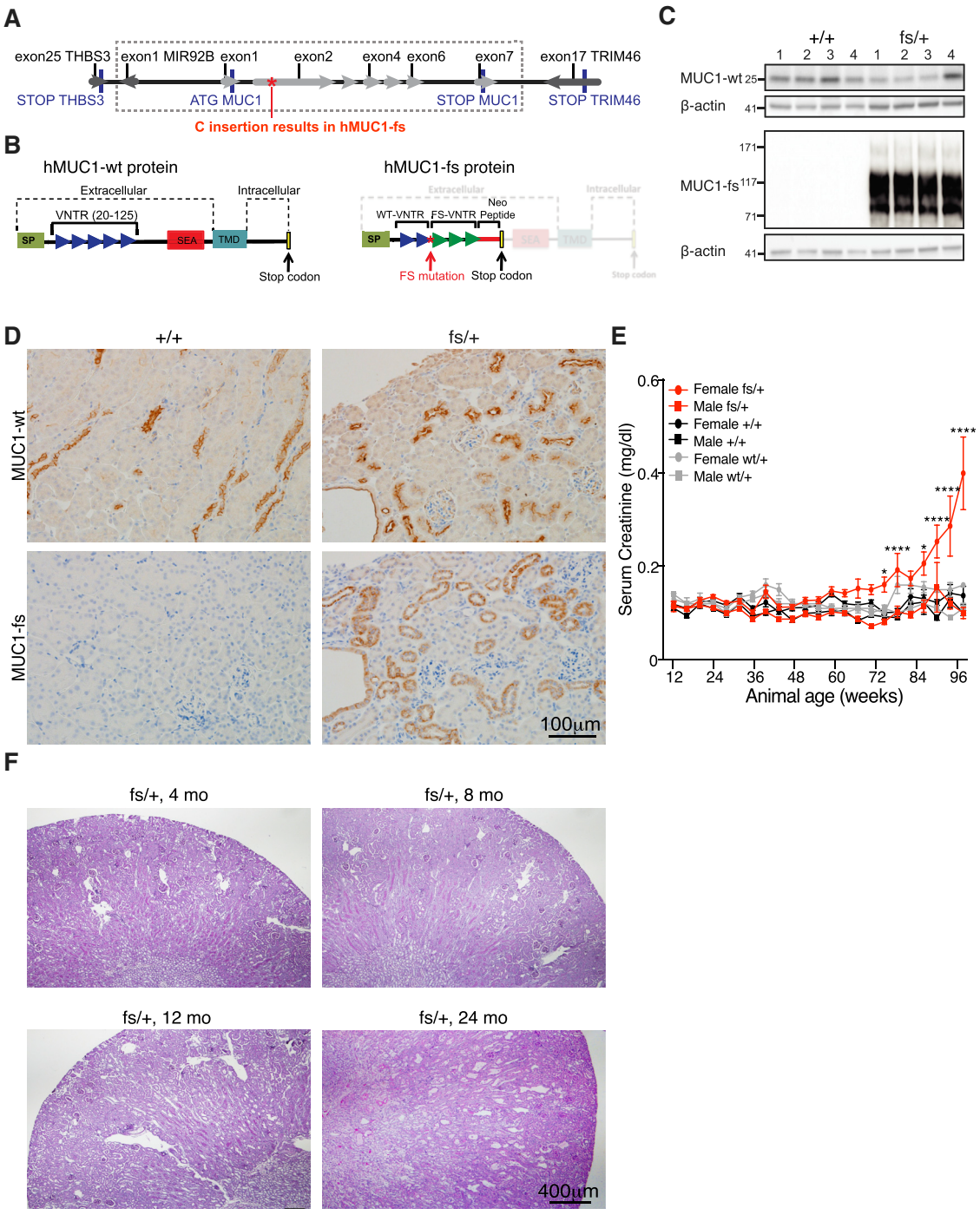

Figure S1. Generation and Characterization of MUC1-fs Knockin fs/+ Mouse, Related to Figure 1

(A) Schematic of *hMUC1-wt* and *hMUC1-fs* genomic constructs (the latter differing only by a single +C (cytosine) insertion (red asterisk) in exon 2) used to generate the wt/+ and fs/+ knock-in mouse models. Box (gray dotted line) shows extent of knock-in fs human gene sequence.

(B) Schematics of hMUC1-wt (left) and hMUC1-fs (right) proteins encoded by the mouse knock-in transgene transcripts. SP, signal peptide. VNTR, variable number of tandem repeats. SEA, sperm protein enterokinase and agrin domain. TMD, trans membrane domain; fs-VNTR, mutant neosequence VNTR; Neo-peptide, unique neosequence C-terminal to the FS-VNTR.

(C) Immunoblot analysis of MUC1-wt and MUC1-fs expression in whole kidney lysates from +/+ and fs/+ KI mice (n = 4 replicates).

(D) Immunoperoxidase staining for MUC1-wt (top) and MUC1-fs (bottom) in kidney sections from +/+ and fs/+ KI mice.

(E) Serum creatinine levels in +/+, wt/+ and fs/+ mice as function of age and gender. Means ± SEM. *Statistically significant difference between fs/+ females +/+ females (for number of animals tested, please refer to Table S1). *$p < 0.05$; ****$p < 0.0001$.

(F) PAS-stained kidney sections from male fs/+ mice at ages 4, 8, 12 and 24 months, illustrating disease progression (n = 20 mice).

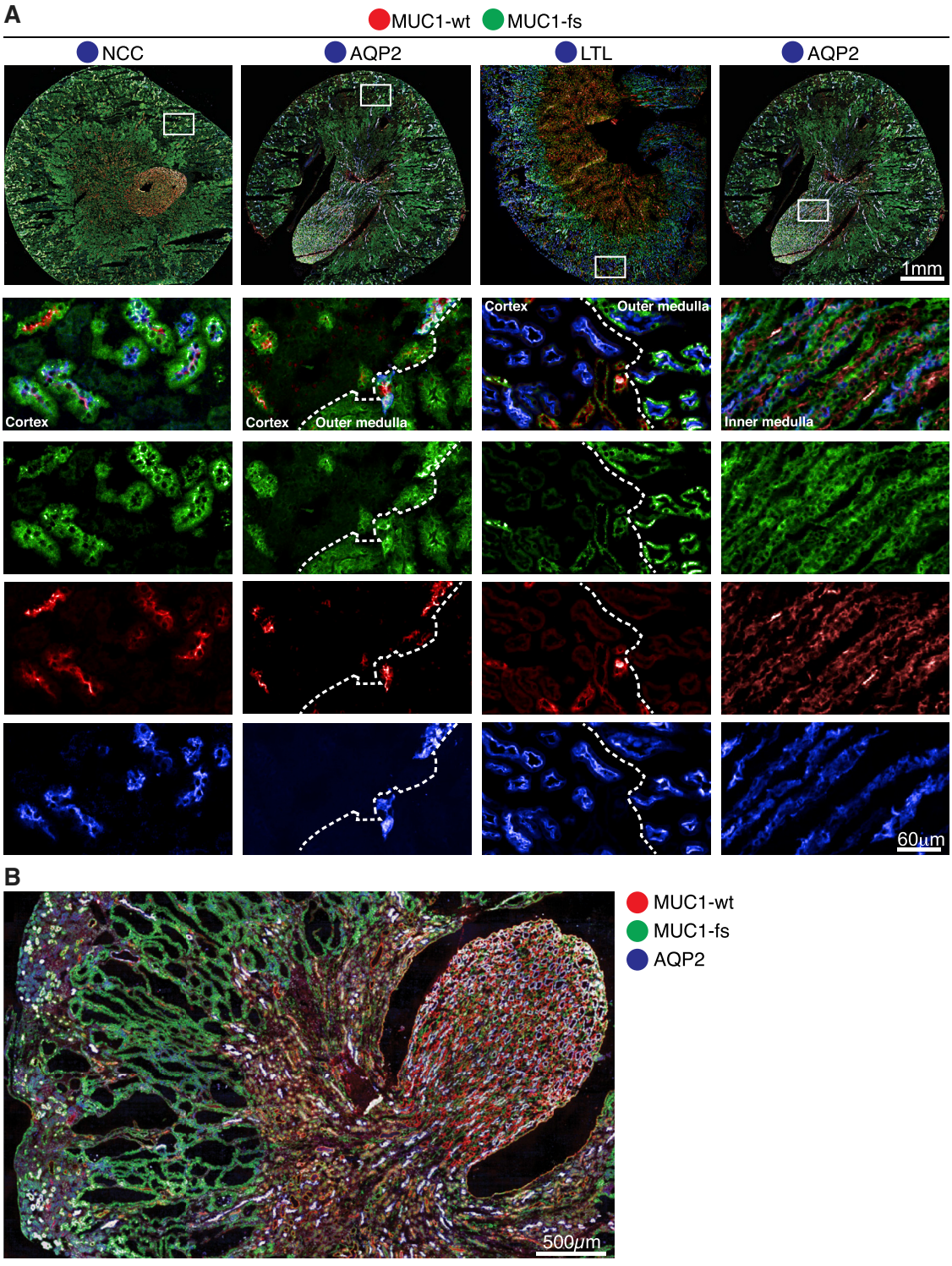

Figure S2. MUC1-fs and MUC1-wt Distribution in Different Segments of Kidneys of fs/+ Mouse, Related to Figure 1

(A) IF images demonstrate the distribution of MUC1-wt (red) and MUC1-fs (green) in kidneys of 4 month old female fs/+ mice. Top, low magnification of an entire kidney section, showing the location of the subsequent high magnification images presented in the bottom rows. First column, co-staining with NCC (blue) in cortex showing distal convoluted tubules positive for both, MUC1-fs and –wt. Second column, co-staining with AQP2 (blue) in cortex and outer stripe of the outer medulla showing collecting ducts positive for both, MUC1-fs and –wt. Third column, co-staining with LTL (blue) in cortex and outer stripe of the outer medulla

(legend continued on next page)

showing lack of MUC1 staining with LTL-positive proximal tubules in the cortex (S1/S2) and positive MUC1-fs staining in proximal S3 tubules in the outer medulla (no MUC1-wt is detected). Fourth column, co-staining with AQP2 (blue) in inner medulla showing collecting ducts positive for both, MUC1-fs and –wt.
(B) IF image of a coronal section from a 24 month old female fs/+ mouse, showing distributions of MUC1-wt (red), MUC1-fs (green) and AQP2 (blue). Note severely dilated tubules, particularly in the outer medulla are associated with high expression of MUC1-fs (green).

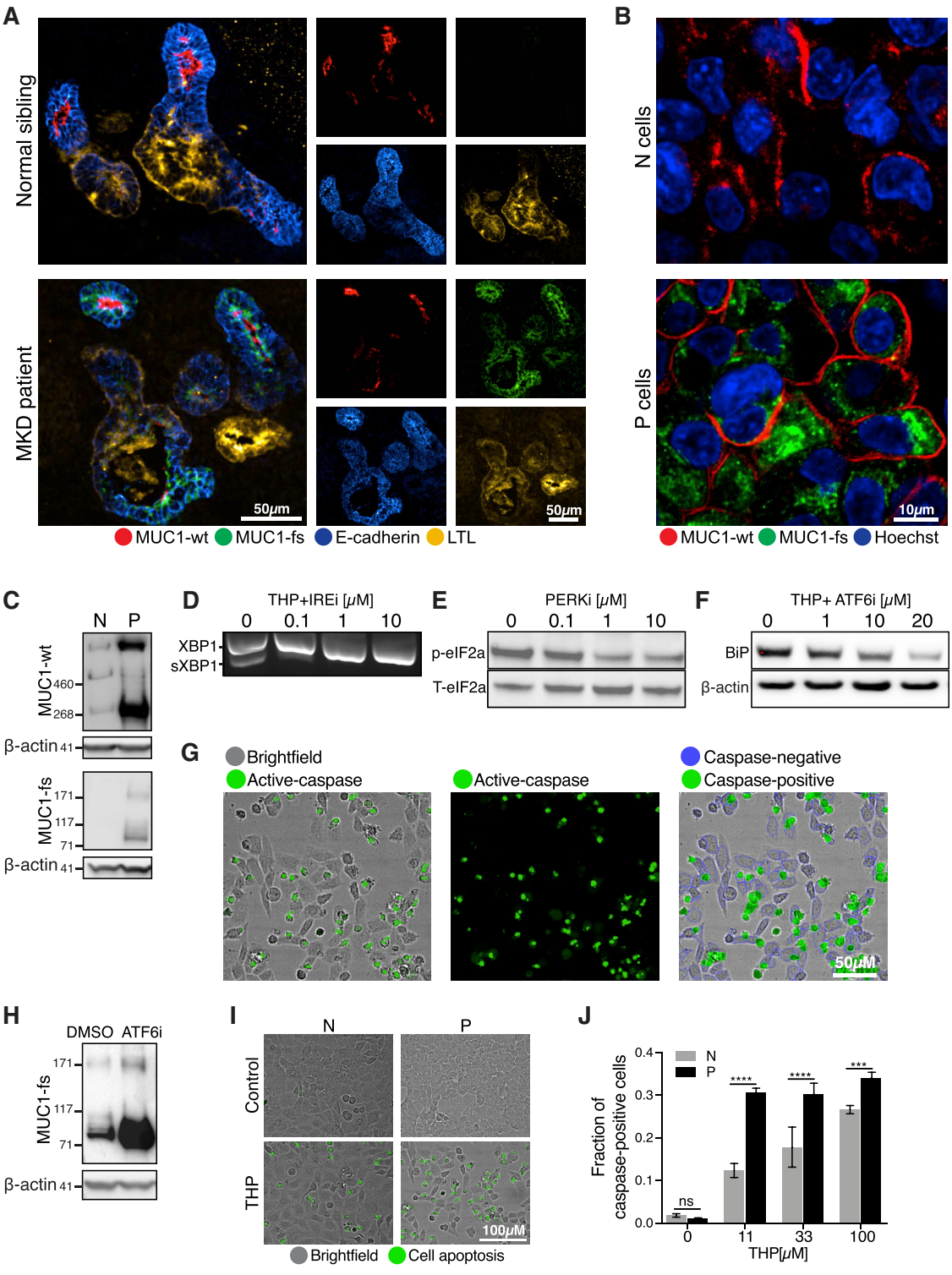

Figure S3. Generation and Characterization of MKD Patient Kidney Organoids and Immortalized Tubular Epithelial Cell Lines, Related to Figures 1 and 2

(A) IF images of human kidney organoids derived from iPSC cells from a normal sibling or an affected MKD patient. Distribution of MUC1-wt (red) and MUC1-fs (green) is shown in proximal and distal tubular structures, marked by LTL (yellow) and by E-cadherin (blue), respectively.

(legend continued on next page)

(B) IF images of normal kidney-derived epithelial cells (N) and MKD patient kidney-derived epithelial cells (P). Co-staining for MUC1-fs (green), MUC1-wt (red) and Hoechst (blue) shows that MUC1-fs is exclusively expressed in P cells and localized intracellularly compared to MUC1-wt, which is expressed in both cell lines and is localized to the plasma membrane.
(C) Immunoblot analysis of MUC1-wt and MUC1-fs proteins in N and P cells shows MUC1-wt expression in both cell lines while MUC1-fs is expressed only in P cells (n = 5 replicates).
(D) RT-PCR analysis of P cells treated with THP (100 nM) shows that IRE inhibitor (IREi, 4μ8c) inhibits IRE activation, as detected by dose- dependent inhibition of XBP1 splicing (sXBP1).
(E) Immunoblot analysis of eIF2a in P cells shows that PERK inhibitor (PERKi, GSK2656157) inhibits PERK activation, as detected by dose- dependent reduction of eIF2a phosphorylation (p-eIF2a).
(F) Immunoblot analysis of BiP in P cells treated with THP (100 nM) shows that ATF6 inhibitor (ATF6i, PF-429242) inhibits ATF6 activation, as detected by dose-dependent reduction of BiP abundance.
(G) Quantitative live imaging analysis sequence of caspase 3/7 activation. Following image acquisition (left panel) single cells are first identified using the digital phase contrast channel and cell number is calculated. Green fluorescence intensity is then measured using 488 channel (middle panel) and the threshold for caspase 3/7-positive staining is determined. As an output, the fraction of caspase 3/7-positive apoptotic cells (right panel, green) or caspase 3/7-negative live cells (right panel, blue) is calculated in each well at each time point.
(H) Immunoblot analysis of MUC1-fs in P cells shows MUC1-fs accumulation following ATF6 inhibition (ATF6i, 10 μM) for 24 h (n = 3 replicates).
(I) Bright field images of representative N and P cells treated with DMSO or THP (33 nM) overlaid with images of caspase 3/7 activation (apoptosis, green) show reduced cell number and increased proportion of caspase positive P cells (quantification is shown in J).
(J) Higher susceptibility of P cells to THP-induced apoptosis after 72 h treatment with indicated concentrations of THP. Cell apoptosis was calculated using the protocol summarized in Figure S3G. Means ± SD (n = 4 replicates) ns, $p > 0.05$; ***$p < 0.001$; ****$p < 0.0001$.

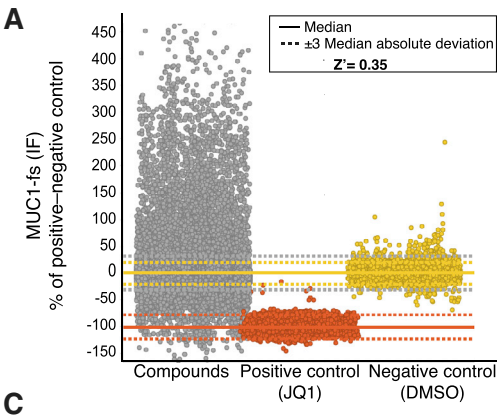

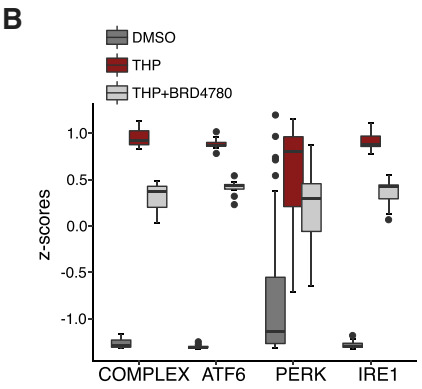

C

		Plasma			Kidney			Kidney/Plasma	Kidney/Plasma	Protein Binding (% bound)	Free Fraction
		AUC	$T_{1/2}$	C_{max}	AUC	$T_{1/2}$	C_{max}	C_{max}	AUC		
		μmol/L.hr	hr	μmol/L	μmol/L.hr	hr	μmol/L				μmol/L.hr
BRD4780	10 mg/kg	47.61	2.18	11.09	1011	2.46	149.4	13.47	21.24	29.7%	711
BRD4780	20 mg/kg	96.07	3.07	14.37	2055	2.43	220.96	15.38	21.39		1445
BRD4780	50 mg/kg	233.14	5.33	26.93	4202	4.71	322.74	11.98	18.02		2954

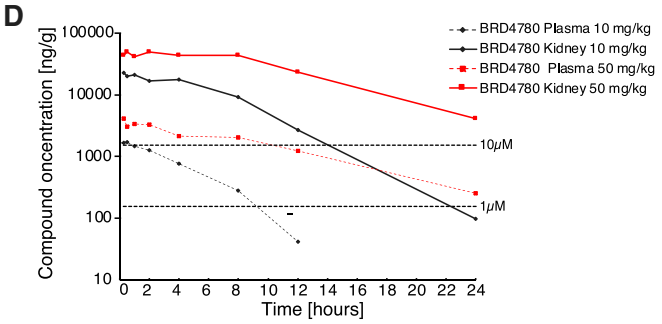

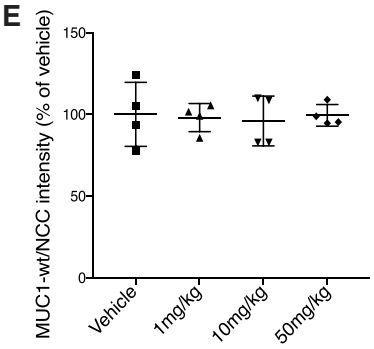

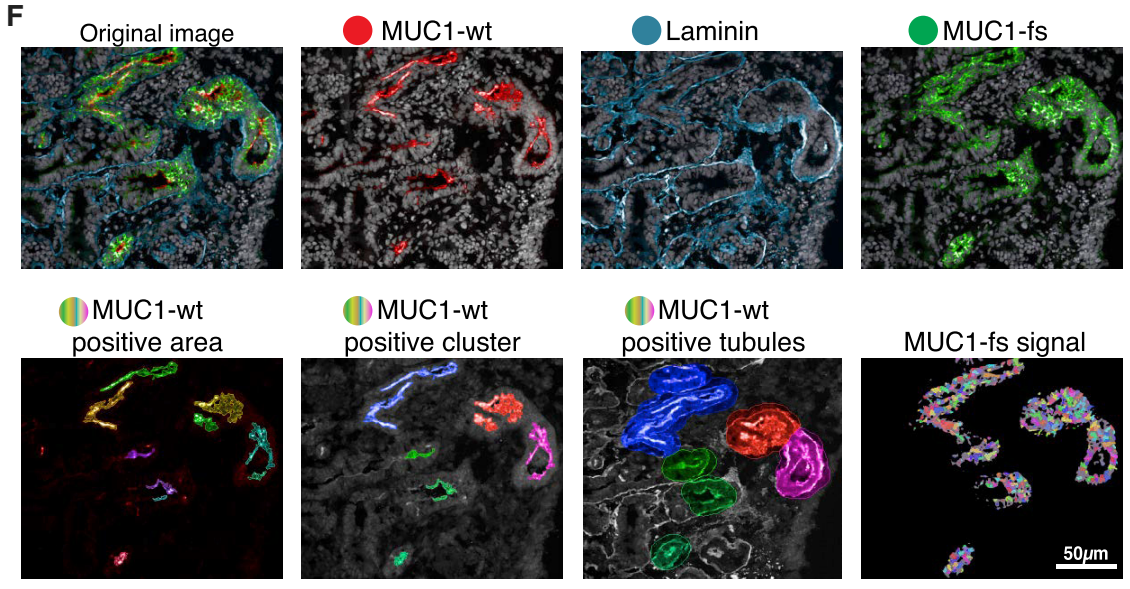

Figure S4. BRD4780 Removes Mutant MUC1-fs from Kidneys of Heterozygous Knockin Mice and Human iPSC-Derived Kidney Organoids, Related to Figures 3–5

(A) Primary screen statistics showing the median and ± 3 median absolute deviations for MUC1-fs IF quantification. Broad Repurposing Library 3713 compounds (gray), DMSO negative control (orange) and JQ1 positive control (yellow). The Z' score statistic for this high content assay was 0.35.

(legend continued on next page)

(B) RNA-Seq analysis of UPR branch activation (as in Figure 2A) in P cells pretreated with DMSO or BRD4780 (1 μM) for 12 h, followed by 12 h co-treatment with THP (100 nM) (n = 3 replicates).
(C) Pharmacokinetic (PK) study in male 129S2 mice following a single oral administration of the indicated doses of BRD4780. Cmax, maximum concentration. AUC, area under curve.
(D) Plasma and kidney tissue concentration of BRD4780 following a single oral administration in male 129S2 mice.
(E) Mean MUC1-wt IF intensity in NCC-positive cells in kidney sections from fs/+ mice treated with vehicle or BRD4780 (1,10 and 50 mg/kg) for 7 days. Means ± SD (n = 4 mice/genotype/dose).
(F) Quantitative region-of-interest IF analysis sequence performed in Figure 5B and 5C. Image acquisition of an entire organoid section (original image of a single field), was done for MUC1-fs (green), MUC1-wt (red) and laminin (blue) staining. MUC1-wt positive regions were identified using MUC1-wt staining (red) with a threshold of > 7000 intensity and > 2500 μm^2. MUC1-wt mean intensity was subsequently calculated in these regions and averaged for the entire organoid section. MUC1-wt regions, which were < 5μm apart, were clustered together and an area of 20 μm surrounding these clusters was selected as a MUC1 positive tubule. MUC1-fs signal was then detected using a spot identifier within these tubules excluding laminin area; the mean intensity of FS signal was calculated there and averaged for the entire organoid section.

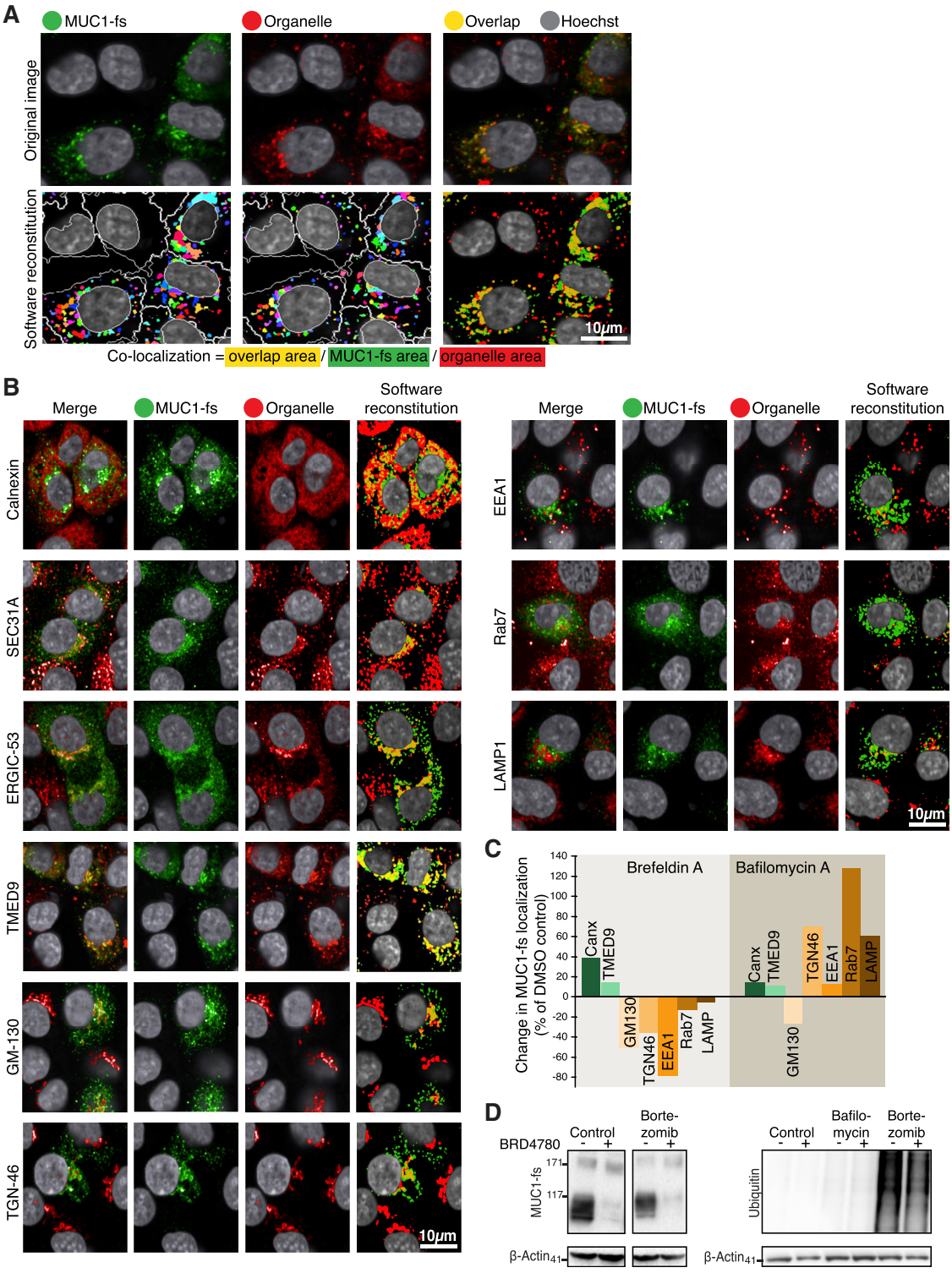

Figure S5. MUC1-fs Accumulates in the Early Secretory Pathway, in a TMED9-Cargo Receptor Positive Compartment, Related to Figure 6

(A) IF analysis sequence of MUC1-fs intracellular co-localization in P cells. Following image acquisition of MUC1-fs (green) and organelle (red), single cell cytoplasm was identified (white border lines)(bottom right and middle panels) and the signals of MUC1-fs and the organelle within the cytoplasm was detected and displayed as spots of different colors (bottom left and middle respectively). Overlap between MUC1-fs signal (bottom right, green) and the organelle signal (bottom right, red) was obtained only when pixels of the two signals (green and red) overlapped (bottom left, yellow). Co-localization is then calculated as total overlap area, normalized (divided) to the total area of MUC1-fs, and then to the total area of the organelle.

(legend continued on next page)

(B) Representative IF images of MUC1-fs colocalization with organelle-specific markers (as calculated in Figure 6B). Right panel shows the software reconstruction that was used for downstream measurements (MUC1-fs, green; organelle, red; overlap, yellow).
(C) Effects of BFA and of Bafilomycin A on MUC1-fs subcellular distribution. P cells were treated with BFA (200ng/mL) or Bafilomycin A (100 nM) for 24 h and MUC-fs distribution was tested as described in Figure 6B. Percent change of DMSO treated cells was calculated for MUC1-fs co-localization with each organelle marker (n = 3 replicates). Treatment with BFA resulted in MUC1-fs accumulation in the ER (and reduction in the late secretory pathway i.e., cis- and trans-Golgi, and endosomes). Treatment with Bafilomycin A resulted in accumulation of MUC1-fs in the late secretory pathway, and especially the late endosome/lysosome.
(D) Immunoblot analysis of MUC1-fs in P cells following 5 h inhibition of the proteosome by Bortezomib (50nM) in the absence or presence of BRD4780 (5 μM)(left). Proteasomal inhibition was confirmed in N cells by increased ubiquitin levels after Bortezomib treatment (50nM)(right). Proteosomal inhibition did not affect MUC1-fs removal by BRD4780, indicating that its degradation did not occur in the proteasome. (n = 3 replicates)

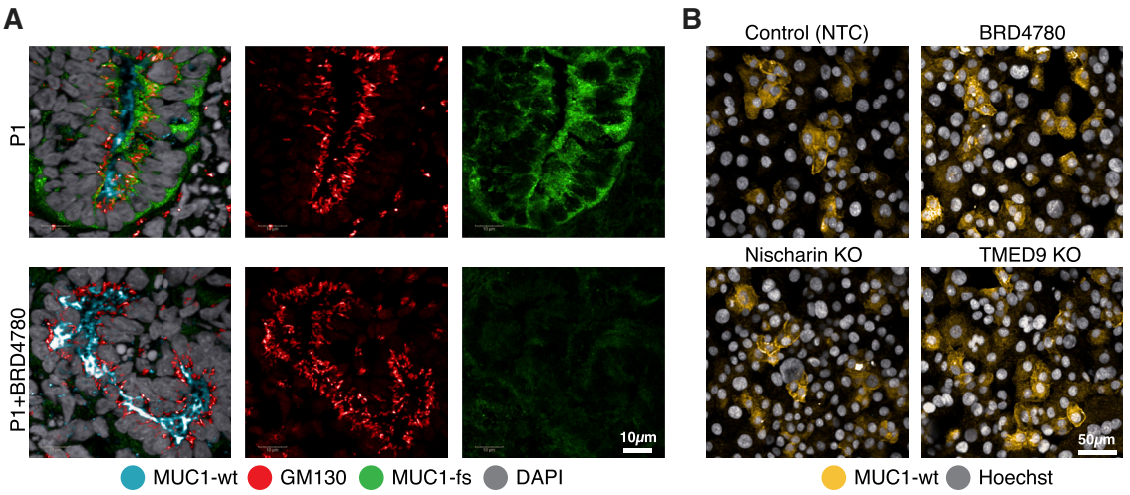

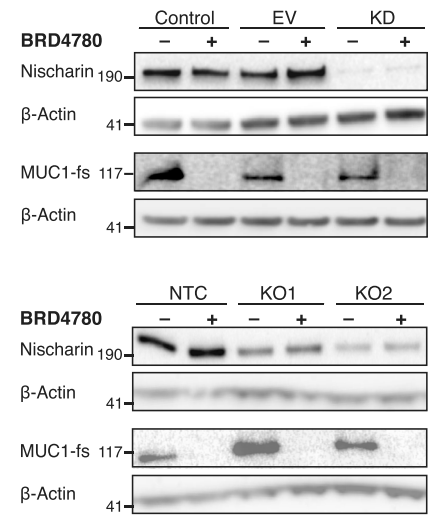

D

Compound Name	MoA	EC50 [M]
BRD4780	?	1,43E -07
Guanfacine	IRL	N/A
Harmine hydrochloride	IRL	N/A
6-Methoxyharmalan	IRL	N/A
Efaroxan hydrochloride	IRL	N/A
Idazoxan	IRL	N/A
tetrahydro -Harmin	IRL	N/A
p-Iodoclonidine hydrochloride	IRL	N/A
Oxymetazoline hydrochloride	IRL	N/A
Agmatine	IRL	N/A
Cirazoline	IRL	N/A
BU 224 Hydrochloride	IRL	N/A
TVP1022	IRL	N/A
Guanabenz acetate	IRL	N/A
Naphazoline hydrochloride	IRL	N/A
Moxonidine hydrochloride	IRL	N/A
Harmaline hydrochloride dihydrate	IRL	N/A
Clonidine	IRL	N/A
Rilmenidine	IRL	N/A

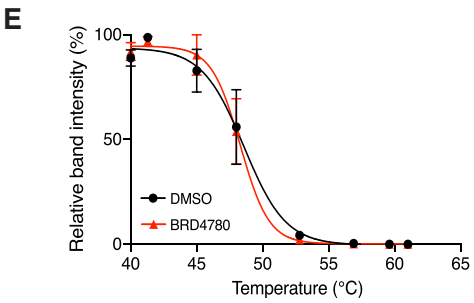

Figure S6. Mechanism of Action of BRD4780 by Engagement of Its Target, the Cargo Receptor TMED9, Related to Figure 7

(A) IF images of MUC1-fs (green), GM130 (red) and MUC1-wt (blue) in MKD patient iPSC-derived kidney organoids showing no change in GM130 abundance upon BRD4780 (10 μM) treatment for 72 h.

(B) IF of MUC1-wt (yellow) and Hoechst (gray) in P cells after TMED9 or Nischarin deletion compared to cells treated with non-targeting sgRNA control (NTC) before and after treatment with BRD4780 (5 μM) for 72 h. No change in either MUC-wt abundance or its plasma membrane localization is observed.

(legend continued on next page)

(C) Immunoblot analysis of P cells after depletion of I1R candidate (Nischarin) using shRNAs (KD1 and KD2; top) or CRISPR-Cas9 deletion (KO1 and KO2; bottom). BRD4780 (5 μM) treatment was applied for 72 h. BRD4780 remains effective despite I1R depletion.

(D) Eighteen compounds annotated as imidazoline-1 receptor ligands (IRLs) and their EC_{50} values for reduction in MUC1-fs levels. Each compound was applied to P cells for 48 h and effects on MUC1-fs were analyzed by IF imaging (N/A, non-active, EC_{50} > 2E-05 [M]).

(E) BRD4780 does not bind Nischarin, as assessed by CETSA. Densitometric analysis of Nischarin abundance after treatment of P cells with BRD4780 (5 μM, 1 h) or DMSO, followed by exposure to escalating temperatures shows no change in nischarin abundance in the presence of BRD4780. Solid lines represent the best fits of the data to the Boltzmann sigmoid. Means ± SEM (n = 3 replicates).

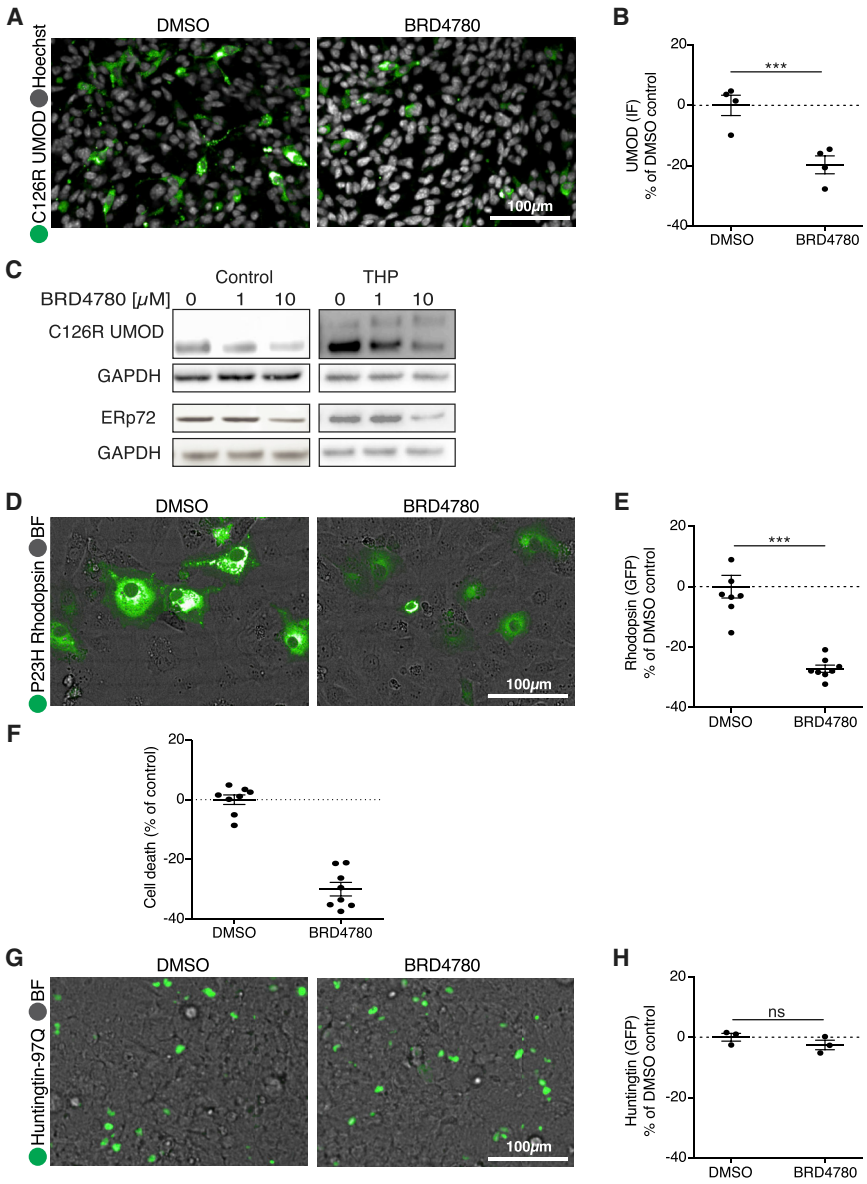

Figure S7. BRD4780 Can Remove Several Misfolded Proteins, Related to Figure 7

(A) IF images of UMOD (green) and Hoechst (gray) in AtT-20 cells stably transfected with C126R-UMOD and treated for 72 h with DMSO or BRD4780 (10 μM).

(B) IF quantification of C126R-UMOD in AtT-20 cells treated as in A. Means ± SD (n = 4 replicates). ***p < 0.001.

(C) Immunoblot analysis of UMOD and ERp72 in AtT-20 cells stably transfected with C126R-UMOD, pre-treated for 24 h with DMSO or BRD4780 (1 μM or 10 μM) and an additional 24 h with THP (10 nM).

(D) Bright field (BF) images (gray), overlaid with images of mutant rhodopsin P23H-GFP (green) in N cells pre-treated for 48 h with DMSO or BRD4780 (5 μM) followed by transient transfection with mutant rhodopsin P23H-GFP.

(E) GFP intensity in live N cells expressing P23H-GFP and treated as in D. See methods for details. Means ± SD (n = 8 replicates). ***p < 0.001.

(F) Fraction of DRAQ7-positive cells (cell death marker) was determined in live N cells transiently transfected with mutant rhodopsin P23H-GFP and treated with DMSO or BRD4780 (5 μM) for 72 h. Means ± SD (n = 8 replicates).

(G) Bright field (BF) images (gray), overlaid with images of huntingtin-GFP containing 97 polyQ repeats (green) in HEK cells transiently transfected with huntingtin-GFP containing 97 polyQ repeats and treated for 72 h with DMSO or BRD4780 (10 μM).

(H) GFP puncta fluorescence intensity of huntingtin protein in live HEK cells expressing huntingtin-GFP and treated as in G. See Methods for details. Means ± SD (n = 3 replicates). ns, p > 0.05.